Excited state dynamics in the strong coupling regime

Jürgen Mony

UNIVERSITY OF GOTHENBURG

Department of Chemistry and Molecular Biology
University of Gothenburg
2022

Doctoral Thesis

Submitted for fulfillment of the requirements for the degree of
Doctor of Philosophy in Chemistry

Excited state dynamics in the strong coupling regime

Jürgen Mony

ISBN: 978-91-8009-677-5 (PRINT)
ISBN: 978-91-8009-678-2 (PDF)

Department of Chemistry and Molecular Biology
SE-412 96 Göteborg
Sweden

Printed by Stema Specialtryck AB
Borås

Abstract

Strong exciton-photon coupling exhibits the possibility to modify photophysical and photochemical properties of organic molecules without changing their structure. This is due to the formation of hybrid light-matter states, called polaritons, which are created when the strong coupling regime is achieved. The polaritons inherit properties from both parts, light and matter, resulting in unique properties.
In this thesis, the excited state dynamics of different strongly coupled systems are presented. The emission lifetime of polaritons were explored by optical spectroscopy. Their emission lifetime showed to be independent of both their excitonic/photonic constitution and the measuring angle. These findings support the theory of the exciton reservoir theory. Furthermore, the impact of strong light-matter interactions on the photoisomerization quantum yield of a photoswitch was examined. The photoisomerization quantum yield showed a dependence whether the system was excited at the lower or upper polariton and on the photonic/excitonic constitution of the polariton. When exciting the upper polariton, the quantum yield was unperturbed whereas it dropped significantly when exciting the lower polariton. Finally, the formation of aggregated states in the strong coupling regime were studied. It was observed that the emission can be controlled by simply altering the photonic and excitonic contribution to the lower polariton. A higher excimer emission was seen for samples, whose lower polariton have a higher excitonic character, whereas a higher photonic contribution resulted in an enhanced polariton emission.
The deeper understanding of the excited state dynamics in the strong coupling regime might result in higher performances in optical applications such as TTA upconversion or singlet fission. Furthermore, the deepened knowledge can unveil the potential of the arising field of polaritonic chemistry.

Acknowledgement

First of all, I would like to thank my supervisor Prof. Karl Börjesson for the opportunity to work as a PhD student in his research group and for all the support throughout all these years. I really appreciated the helpful meetings, whenever I was stuck in my projects. I hope you keep your enthusiasm, it makes you a great supervisor and researcher. I would also like to thank my examiner Prof. Johan Bergenholtz, whose guidance made everything work out quite smoothly, and my co-supervisor Prof. Gunnar Nyman. I'd like to express my gratitude to Assoc. Prof. Jussi Toppari for being my opponent at my thesis defence and to Prof. Maria Abrahamsson, Assoc. Prof. James Gardner, Prof. Mikael Käll and Prof. Joakim Andréasson for being members of the thesis committee.

I'd like to take the opportunity to acknowledge my collaborators, whose contribution made this work possible: Dr. Johannes Feist and Dr. Clàudia Climent for the theoretical input to the photoisomerization project, Clara Schäfer, Dr. Kushbu Kushwaha and Prof. Kasper Moth-Poulsen for providing the molecules in different projects, Yi Yu for the nice collaboration during our last project and Dr. Manuel Hertzog for the modelisation and help with python in my first project.

Many thanks to all the present and past members of the molecular materials group. Especially Arpita, Alex and Pedro, who were my office mates. To all colleagues on the 8^{th} for the nice international dinners.

What would life be without food and friends? I'd like to thank my lunch group Andrew, August, Chen, Clara and Manuel for the small moments of joy even on stressful days. Chen, I really appreciated the dinners and conversations with you, thanks for that. Clara Klara and August, thanks for all the brewed and emptied beer. In general, for all the good times we had together like on Gotland or at Dirty Dough. Manuel, you cannot avoid to

be mentioned here. No Datenschutz, Brudi. I will figure out a way to fax this thesis to you. Yizhou, it's really hard to convince you to join us for tea, but it was always super fun with you. Yongjin, I really enjoyed our hiking trip on kungsleden and all the days we went for swimming.
Betrachtet man die Doktorarbeit als Krönung des Studiums, so darf man den Anfang des Studiums natürlich nicht vergessen. Danke an Jens and Florian für das Durchstehen anstrengender Tage im Labor und den Genuß gemeinsamer Abende im Biergarten.
Darüber hinaus gibt es noch Leute, die ich schon viel länger kenne und deren Freundschaft ich niemals missne möchte. Raphael, vielen Dank für die vielen Runden Rage oder Civ, die mir stets eine benötigte Werbepause für den Alltag waren. Hoffentlich besteht bald mal die Möglichkeit ins Stadion zu gehen, um Aufstiege zu feiern.
Jana, vielen Dank für die langen Telefonate, die einem das Gefühl der Verbundenheit gaben trotz der großen Entfernung zueinander.
Zu guter Letzt bleibt nur der Dank an meine Familie für die Unterstüztung, die mir die Freiheit gewährt, das tun zu können, was ich möchte. Ich freue mich immer darauf mal wieder nach Hause zu kommen.

List of Publications

The work presented in this thesis is based on the research articles referred to as paper **I-III**:

Paper I **Angle-Independent Polariton Emission Lifetime Shown by Perylene Hybridized to the Vacuum Field Inside a Fabry–Pérot Cavity**
Jürgen Mony, Manuel Hertzog, Khushbu Kushwaha and Karl Börjesson, *J. Phys. Chem. C* **2018**, *122(43)*, 24917–24923. [1]

Paper II **Photoisomerization Efficiency of a Solar Thermal Fuel in the Strong Coupling Regime**
Jürgen Mony, Clàudia Climent, Anne Ugleholdt Petersen, Kasper Moth-Poulsen, Johannes Feist and Karl Börjesson, *Adv. Funct. Mater.* **2021**, *31*, 2010737. [2]

Paper III **Interplay between polaritonic and molecular trap states**
Jürgen Mony, Yi Yu, Clara Schäfer, Suman Mallik, Khushbu Kushwaha, and Karl Börjesson, *Manuscript.*

Further research articles, which are not included in this thesis:

Paper i **Strong light–matter interactions: a new direction within chemistry**
Manuel Hertzog, Mao Wang, Jürgen Mony and Karl Börjesson, *Chem. Soc. Rev.* **2019**, *48*, 937 [3]

Paper ii **Entropic Mixing Allows Monomeric-Like Absorption in Neat BODIPY Films**
Clara Schäfer, Jürgen Mony, Thomas Olsson and Karl Börjesson, *Chem. Eur. J.* **2020**, *26*, 14295-14299. [4]

Paper iii **A fine-tuned azobenzene for enhanced photopharmacology in vivo**
Vanessa A. Gutzeit, Amanda Acosta-Ruiz, Hermany Munguba, Stephanie Häfner, Arnaud Landra-Willm, Bettina Mathes, Jürgen Mony, Dzianis Yarotski, Karl Börjesson, Conor Liston, Guillaume Sandoz, Joshua Levitz, and Johannes Broichhagen, *Cell Chemical Biology* **2021**, *28* 1648-1663.e16. [5]

Paper iv **The effect of the aza-N-bridge and push-pull moieties, a comparative study between BODIPYs and aza-BODIPYs**
Clara Schäfer, Jürgen Mony, Thomas Olsson and Karl Börjesson, *Submitted Manuscript.*

Paper contribution

Paper I Prepared all samples and performed all spectroscopic experiments, set up the angle-dependent measurement setup for the emission and the emission lifetime. Analyzed the data and wrote the paper together with the other authors.

Paper II Prepared all samples, performed the optical characterization and made the photoisomerization experiments. Analyzed the experimental data and wrote the paper together with the other authors.

Paper III Prepared all samples and performed all spectroscopic experiments for the prompt emission samples. Analyzed the data and wrote the paper together with the other authors.

Contents

Chapter 1

Introduction

The interaction between light and matter is not only the basis of fascinating concepts like seeing colors but also the foundation of life. In the photochemical process of photosynthesis, the energy of sunlight is converted into energy-rich carbohydrates. This processes is initiated by the absorption of photons of certain energies in chlorophyll. The other photons, which are not absorbed, let the leave appear green. Besides absorption, other processes also lead to the observation of colors in nature; the blue sky is due to scattering in the atmosphere and some minerals can emit photons at certain energies after being excited.
The research interest in light-matter interactions is ranging from exploring the fundamental processes to applications improving our society. In the beginning of the 20^{th} century, basic light-matter interactions like blackbody radiation or the photoelectric effect were out of scope of classical physics. The concepts by Planck, Einstein and others [6–11] describing those phenomena flourished into the development of quantum mechanics. It culminated in the quantum theory of light-matter interaction by Dirac [12]. Since then the research interest in light-matter interactions preserved its fascination and importance. Nowadays a big effort in research is made to solve the society's issue of an increasing energy demand accompanied with a reduction of fossil fuel combustion, which used to be our main source of energy. One approach to solve this issue is to convert sunlight into (storable) energy by light-matter interactions. Several ways are possible like the energy conversion into electrical energy using photovoltaic [13–16] or the energy storage in chemical bonding applied in molecular solar thermal energy stor-

age systems (MOST) [17–22]. In the bright field of photocatalysis the effort is made to mimic nature to obtain artificial photosynthesis, where hydrogen and oxygen are generated from water using sunlight and a photocatalyst [23–25].

A special case of light-matter interactions is strong exciton-photon coupling. This special form is achieved when the interaction between light and matter is to an extend that they cannot be treated as separate entities anymore. It leads to the formation of new hybrid light-matter states, called polaritons, which are separated in energy by the Rabi splitting. Those polaritons exhibit unique optical properties inherited by their photonic or excitonic contribution. The theoretical concept of strong exciton-photon coupling was described by Jaynes and Cummings in 1963 [26] and it took until 1975 until Yakovlev *et al.* provided the first experimental work [27]. The following interest in strong coupling was mainly focused on Rydberg atoms [28–31] and inorganic quantum wells [32–34]. However, strong coupling using organic molecules was first described theoretically by Agranovich *et al.* 25 years ago [35], followed by the experimental demonstration by Lidzey *et al.* one year later [36]. In the following years the interesting in strong coupling using organic molecules arose and benchmarks like room temperature Bose-Einstein condensates [37, 38] and lasing [39] has been set. In the recent ten years, photochemical and chemical reactions as such came into focus of this research field [40–58]. The concept of strong coupling is not only restricted to electronic transition but can be extended to vibrational transitions [59–68], which play a major role in chemical reactions.

The introduction of polaritons lead to a rearrangement of the excited state energy levels as well as to altered dynamics [69–77] in comparison to the bare organic molecule case. Therefore, the main focus of this thesis is on the excited state dynamics of strongly coupled systems. The goal of the work was to get a deeper insight in those dynamics to unveil the full potential of strong coupling. An improved understanding might lead to an increased applicability in fields of polaritonic chemistry or optical applications such as triplet-triplet annihilation upconversion, singlet fission or organic electronics.

This thesis is structured into 5 chapters. After the introduction, the basic principles of light-matter interactions are described in chapter 2. It begins with the description of light and its interaction with a two level system. Fol-

lowed by the photophysical processes occurring in an organic molecule. The chapter finishes with a short introduction to photochemical reaction concepts. Chapter 3 starts by explaining the basic principles of strong exciton-photon coupling in a classical, semiclassical and full quantum picture. The description of the main characteristics such as anticrossing, hybridization and energy splitting is included in that first part as well. It is followed by the summary of papers **I-III**, which is the foundation of my work. Thereafter, chapter 4 describes the experimental methods, which were used for sample preparation and optical characterization. Finally, this thesis is summarized and a outlook is provided in chapter 5.

Chapter 2

Fundamental Light-Matter Interactions

2.1 Basic principles

2.1.1 Electromagnetic waves

Light is an electromagnetic wave, which can be classically described by Maxwell's equations [78]. As it might be already concluded by the name, an electromagnetic wave consists of an oscillating electric and magnetic field, which are synchronized. They can be characterized by either their oscillating frequency or their wavelength. In the electromagnetic spectrum they are classified by wavelength into infrared, visible, ultraviolet, X-rays and others. To explain the photoelectric effect [79], light was proposed to be a discrete energy packet [6], which was later called a photon [80]. The energy of a photon is described by its frequency ν and Planck's constant h [9] or, alternatively, by its angular frequency ω and the reduced Planck's constant $\hbar$

$$E = h\nu = \hbar\omega \tag{2.1}$$

A simple case of light-matter interactions is the absorption or emission of a photon by an atomic system having stationary energy levels. According to the Bohr frequency condition [7], the energy difference of the two involved energy states needs to be equal to the frequency of the radiation multiplied

by Planck's constant.

$$\Delta E = h\nu = \hbar\omega \tag{2.2}$$

In optical spectroscopy of electronic states, the wavelength λ is commonly used and therefore the Bohr condition can be rewritten using the speed of light c to

$$\Delta E = \frac{hc}{\lambda} \tag{2.3}$$

2.1.2 Blackbody radiator

A blackbody radiator is a object, which shows a radiation spectrum depending on its temperature (Fig. 2.1). The name blackbody radiator might seem contradictory considering the fact that it is used to describe the solar spectrum. However, the name is based on the idea that all radiation from external sources is absorbed excluding all transmission or reflection. Therefore, the blackbody radiator appears black at room temperature having a thermal radiation spectrum in the invisible IR. The problem of light-matter interaction occurring for a blackbody radiator were out of scope for classical physics. Planck was the first to determine the blackbody radiation spectrum (Fig. 2.1) by the following equation known as Planck's law [10]

$$\rho(\nu) = \frac{8\pi h\nu^3}{c^3} \frac{1}{e^{h\nu/k_B T} - 1} \tag{2.4}$$

the spectral radiation density $\rho(\nu)$ only depends on the temperature T, the frequency ν and physical constants like the speed of light c, Planck's constant h and Boltzmann constant k_B. The intensity peak shifts to higher frequencies or lower wavelength for higher temperatures.

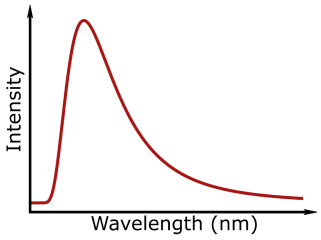

Figure 2.1: Blackbody raditation spectrum according to Planck's law.

2.1.3 Einstein coefficients

Einstein postulated three possible processes for the interaction between a photon and a two level system (Fig. 2.2), which consists of two discrete energy levels separated in energy [11]. The first one is the absorption where the system gets excited after absorbing a photon. The change of the excited state population over time $\frac{dN_n}{dt}$ for this process can be described by

$$\frac{dN_n}{dt} = N_m B_{mn} \rho(\nu) \tag{2.5}$$

where N_m is the population of ground state m, B_{mn} is the Einstein coefficient of absorption and $\rho(\nu)$ is the spectral density at the frequency of radiation. The non-intuitive stimulated emission is the second process and works in a reverse way to absorption. A photon stimulates the emission of another photon from an excited two level system. The depopulation of the excited state over time is determined by

$$\frac{dN_n}{dt} = -N_n B_{nm} \rho(\nu) \tag{2.6}$$

where N_n is the population of excited state n and B_{nm} is the Einstein coefficient of stimulated emission. As a consequence of the competing processes of stimulated emission and absorption, no population inversion of a two level system can be achieved.

The third process is the spontaneous emission, where a two level system relaxes down to its ground state by emitting a photon. In contrast to the other two processes, the spontaneous emission is independent of any photon radiation and only depends on the Einstein coefficient for spontaneous emission A_{nm} and the population of the excited state N_n

$$\frac{dN_n}{dt} = -N_n A_{nm} \tag{2.7}$$

The relation between the Einstein coefficients of the spontaneous and stimulated emission can be obtained from the steady-state condition. In this regime the populations of the ground state and excited state are in equilibrium. Using Planck's law for the spectral radiation density the relation is determined as

$$A_{nm} = \frac{8\pi h\nu^3}{c^3} B_{nm} \tag{2.8}$$

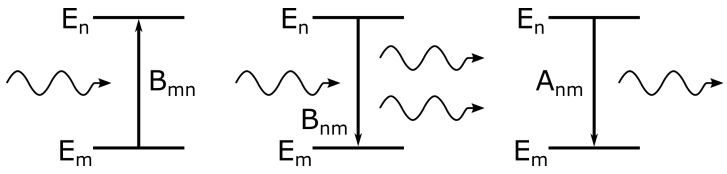

Figure 2.2: Three processes: Absorption, stimulated emission and spontaneous emission in a two level system with the ground state m and the excited state n.

2.1.4 Rabi oscillation

Rabi oscillations appear in quantum two level systems, which interact with an external electromagnetic wave [81]. If the excitation frequency of the electromagnetic field is close to the resonant frequency of the two levels, the system starts to oscillate between the ground and excited state with the Rabi frequency Ω_R

$$\Omega_R = \frac{d|E_0|}{\hbar} \tag{2.9}$$

where d is the associated transition dipole moment and E_0 is the amplitude of the electric field.

Using the wavefunction describing the excited and ground state, the population probability can be obtained for each state. Assuming that the system is initially in its ground state the probability of the system being in the excited state is

$$P_e(t) = \frac{\Omega_R}{\sqrt{\Omega_R^2 + \delta^2}} sin^2 \frac{\sqrt{\Omega_R^2 + \delta^2}}{2} t \tag{2.10}$$

where $P_e(t)$ is the probability to be in the excited state and δ is the detuning between the frequency of light and the frequency of the transition between ground and excited state. The probability to be in the excited state is oscillating over time, which means that continuous excitation of a two level system doesn't result in the system being in the excited state all the time (Fig. 2.3). After the excitation is created, further excitation brings the system to its ground state due to stimulated emission. The detuning effects the probability as well as the frequency of the oscillation (Fig. 2.3). Only for the case of no detuning, the probability to be in the excited state reaches

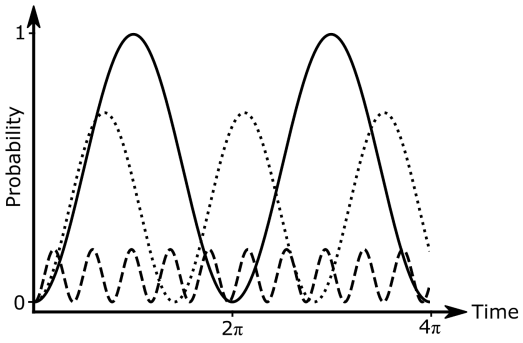

Figure 2.3: Rabi oscillation in the probability P_e over time using different detuning of $\delta = 0$ (straight line), $\delta = \Omega_R$ (dotted line) and $\delta = 5\Omega_R$ (dashed line)

unity at certain times. Furthermore, when the external excitation is shut off the system stays in the same state. This is a very simplified model since it doesn't take any decays, relaxation or dephasing into account.

2.2 Photophysical processes in molecules

Molecules are not just simplified two level systems. The energetic structure consists of many different levels and many different types of transitions, which all are induced by light. This section starts by introducing electronic and vibrational states of organic molecules. Followed by their interaction with a photon and the subsequent processes of the excited state.

2.2.1 Electronic states

The electronic energy levels of organic molecules can be calculated by the time-independent Schrödinger equation [82].

$$\hat{H}\Psi = E\Psi \tag{2.11}$$

where $\hat{H}$ is the Hamiltonian operator, Ψ is the eigenfunction and E is the total energy, which can be split up in kinetic energy, potential energy and the electron-electron interaction energy. The Schrödinger equation can only be solved analytically for the hydrogen atom having one electron and thus no electron-electron interaction energy [83]. From that calculation the dif-

ferent atomic orbitals, namely s,p and d-orbitals, can be seen. Following the Aufbau principle atomic orbitals are filled with electrons starting at the one with the lowest energy. The Schrödinger equation for many electron systems can only be approximated. The determination of molecular orbitals are normally determined for each electron independently [84]. Molecular orbitals are a linear combination of different atomic orbitals. The highest occupied molecular orbital (HOMO) and the lowest unoccupied molecular orbital (LUMO) play the most important role for photophysical and photochemical processes.

2.2.2 Vibrational states

Molecules exhibit many vibrational states within each electronic state. The number of possible vibrations is determined by their degree of freedom, which is $3N-5$ for linear molecules and $3N-6$ for other molecules, where N is the number of atoms in the molecular structure. Considering a two atomic molecule as the simplest case, only one vibration is allowed. The potential energy surface can be described by a harmonic oscillator.

$$V(x) = -kx^2 \tag{2.12}$$

with the spring constant k and the spatial distortion x. Solving the Schrödinger equation leads to the energy eigenstates of the vibrational level E_v [83]

$$E_v = \hbar\omega(v + \frac{1}{2}) \tag{2.13}$$

where v is the vibrational quantum number. From the equation can be seen that the energy levels are equidistant and never zero. In reality the potential energy surface does not behave like a perfect oscillator. Having a classical picture of two atoms connected by a spring in mind, it is obvious that at some level of distortion the spring and thus the bond will break. The harmonic oscillator is also not valid for bringing the two positively charged nuclei too close together. At some level of approximation the Coulomb repulsion will start to play a major role. As a correction factor for the potential energy surface, the Morse potential is introduced [85] (Fig. 2.4).

$$V(r) = D_e(1 - e^{-a(r-r_e)})^2 \tag{2.14}$$

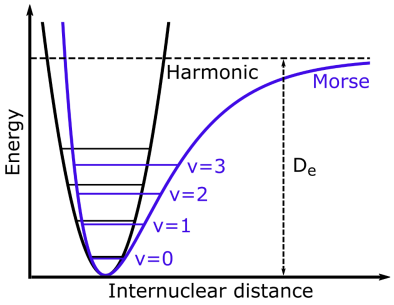

Figure 2.4: Energy scheme of the Morse potential (blue) in comparison with the harmonic oscillator (black) with several vibrational levels and the dissociation energy D_e

where $V(r)$ is the Morse potential, D_e is the dissociation energy, $r - r_e$ is the distortion and a is a parameter containing the spring constant k

$$a = \sqrt{\frac{k}{2D_e}} \tag{2.15}$$

The corrected potential energy is accompanied by a shift in the vibrational energy levels, which are not equidistant anymore. Nevertheless, it remains a good approximation to assume the lowest vibrational levels to be uniformly separated.

2.2.3 Molecular absorption

Perrin-Jabłonski digram

The electronic and vibrational energy levels of an organic molecule play an important role for optical properties. The energy transitions between those levels can be summarized in a Perrin-Jabłonski diagram [86] (Fig. 2.5). The different processes can be divided up into radiative and non-radiative. Absorption, fluorescence and phosphorescence are radiative processes whereas intersystem crossing (ISC), internal conversion (IC) and vibrational relaxation are non-radiative processes. This subsection will start describing the absorption and its characteristics followed by the interactions and processes in the excited state.

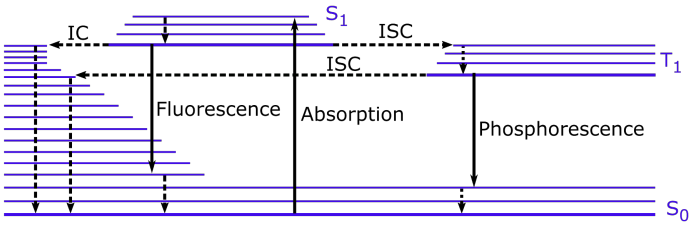

Figure 2.5: Perrin-Jabłonski diagram of the photophysical processes within an organic molecule. The thick blue lines represents the electronic levels and the thin blue lines the vibrational levels. Radiative transitions like absorption, fluorescence and phosphorescence are indicated by straight lines and non-radiative processes like IC, ISC and vibrational relaxation are indicated by dashed lines.

Transition probability

The electric field of light can interact with the charged electrons and nuclei of a molecule. For absorption to occur, the Bohr frequency condition needs to be met as a first requirement, which says that the energy of the photon needs to match with the energy difference between two electronic states. This condition does not give any insights on how probable a transition between the two states is. Therefore, we need to consider the electric dipole moment operator $\boldsymbol{\mu}$, which is defined as [87]

$$\boldsymbol{\mu} = \sum_i q_i \mathbf{r_i} \tag{2.16}$$

where q_i is the charge and the position of the i^{th} particle. The position $\mathbf{r_i}$ is a vector based on the Cartesian position x, y and z. It is used to obtain the transition moment $\mathbf{d_{fi}}$ between an initial state Ψ_i and the final state Ψ_f

$$\mathbf{d_{fi}} = \int \Psi_f^* \hat{\mu} \Psi_i d^3\mathbf{r} \tag{2.17}$$

The transition probability P is then:

$$P \propto |\int \Psi_f^* \hat{\mu} \Psi_i d^3\mathbf{r}|^2 \tag{2.18}$$

The transition probability and thus the intensity is related to selection rules; it is non-zero for an allowed transition and zero for a forbidden transition. According to selection rules a transition can be either spin-forbidden or

symmetry forbidden.
In the case of the spin selection rule, the overall multiplicity needs to be conserved for a transition [88]. Therefore, the $S_1 \leftarrow S_0$ or $T_n \leftarrow T_1$ transitions are allow, whereas the transition from a singlet to a triplet state is forbidden due to the spin flip. This spin selection rule can be violated by the spin-orbit coupling, where the spin and orbital function cannot be separated anymore [89, 90]. The strength of the spin-orbit coupling increases with the atomic number, which is often called the heavy atom effect. In that sense even a spin forbidden transition can be turned into a spin allowed transition enabling phosphorescence and intersystem crossing (ISC).
The symmetry selection rule, also called Laporte rule [91], applies for centrosymmetric molecules [83]. The only allowed transition is when the parity changes, which is the case when the molecule goes from a symmetric state with respect to the inversion center to an antisymmetric state or vice versa. A transition with conserved parity can become weakly allowed when the centre of symmetry is lost due to an antisymmetrical vibration of the molecule.

Vibronic transitions

Considering the structure of an absorption spectrum having different vibrational and electronic levels, the populated level of the molecules before excitation needs to be known first. It can be determined using the Boltzmann distribution law [83]

$$\frac{N_0}{N_v} = e^{\frac{\Delta E}{k_B T}} \tag{2.19}$$

where N_0 and N_v are the population of the lowest vibrational state and the v^{th} energy state, respectively; ΔE is the energy difference between the vibrational states, k_B is the Boltzmann constant and T is the temperature. Normally, the energy difference between vibrational levels exceeds the factor $k_B T$ at room temperature and therefore the majority of molecules are in the lowest vibrational level. Using the Born-Oppenheimer approximation that the electronic eigenfunction and the vibrational eigenfunction can be treated independently [92], it can be concluded that the probability and therefore the intensity of a vibronic transition only depends on the overlap between the wavefunctions of the lowest vibrational level of the ground

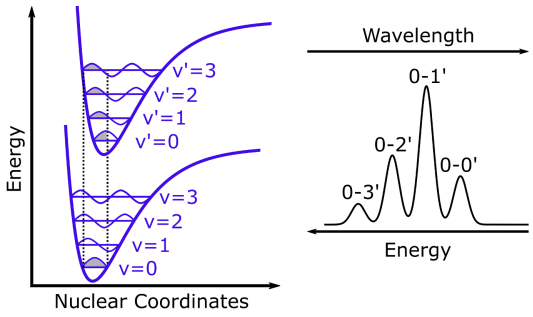

Figure 2.6: Energy scheme with the ground state and excited state indicating the wavefunctions of the vibrational level and the Franck-Condon overlap integrals. Absorption spectrum showing the different vibronic transitions according to the Franck-Condon principle [93, 94].

state and the vibrational level of the excited state (Fig. 2.6). The higher the overlap the higher is the transition probability [93, 94]. Those overlaps are called Franck-Condon integrals. The result is an absorption spectrum having different intensities for different vibronic transitions.

Spectral broadening

Although the absorption is a transition between discrete energy levels, the measured spectrum does not resemble a straight line due to different kinds of broadening. The natural broadening is a result of the Heisenberg's uncertainty principle [95, 96] and the short lifetime τ of the final excited states [87].

$$\Delta E\tau \geq \hbar \quad or \quad \Delta\nu\tau \geq \frac{1}{2\pi} \tag{2.20}$$

from the equation can be seen that the broadening (ΔE or $\Delta\nu$) only depends on the lifetime of the final state and the shorter it is the wider is the broadening. The broadening results in a characteristic Lorentzian line shape. However, the natural line broadening is usually very small compared to other causes of broadening.

When dye molecules are integrated into a solid host matrix, the inhomogeneous broadening plays an important role in the broadening [97]. The surrounding of the molecule can determine the exact energy level of the electronic state due to local defects, dislocations or impurities [98]. Therefore, the transition energies of the molecules differ slightly in dependence

on their surrounding. This leads to a broadening with a Gaussian shape.
The Doppler effect also leads to a spectral broadening. It is based on the movement of the atom or molecule relative to the detector and depends on their relative velocities [87].

$$\Delta\nu = \frac{\nu}{c}\left(\frac{2k_BTln2}{m}\right)^{1/2} \tag{2.21}$$

where c is the speed of light, ν is the frequency of the transition, k_B is the Boltzmann constant, T is the temperature and m is the mass of the atom or molecule. The broadening leads to a Gaussian shaped line width, which is usually observed in absorption spectra.
Pressure broadening is the fourth line shape broadening process. It occurs due to the collision between atoms or molecules in the gas phase resulting in an exchange of energy and therefore in a line shape broadening $\Delta\nu$ of [87]

$$\Delta\nu = \frac{1}{2\pi t} \tag{2.22}$$

where t is the mean time between collisions.

2.2.4 Processes in the excited state

Non-radiative processes

The fastest non-radiative process is the vibrational relaxation [99]. During this process the molecule relaxes from a higher vibrational level to the lowest one within the same electronic state. The excess of energy is released to the surrounding. Vibrational relaxation occurs, for example, subsequently to the excitation of a molecule to a higher vibrational level in the excited state. Since vibrational relaxation is the fastest proces, the molecule relaxes back to the lowest vibrational level from where it will undergo other radiative or non-radiative processes. So, molecules are rarely found in higher vibrational level due to the vibrational relaxation.
Another non-radiative process is the internal conversion (IC) [99]. In contrast to the vibrational relaxation the IC changes its electronic state. This process is usually irreversible since it is followed by the very fast vibrational relaxation, which brings the molecule down to the lowest vibrational level. Together with the vibrational relaxation it is the reason for Kasha's rule,

which states that for a given multiplicity the luminescence only comes from the lowest excited state [100]. This means that the fluorescence is independent of the excitation wavelength. This is caused by the fact that the IC and vibrational relaxation in the excited states are faster than the luminescence from higher excited states. The fluorescence rate constant can only compete with the IC from the lowest excited state, which is a consequence of the energy gap law. According to this law the rate constant of a non-radiative decay as IC and ISC decreases exponentially as the energy difference between two electronic states increases in a series of related molecules. There are two competing processes for this observation: On the one hand the rate constant from the initial to the final electronic state $k_{i\to f}$ should increase due to Fermi's law (Eq. 2.23) since the density of vibrational states in the final electronic state ρ_f is higher for bigger energy gaps [101].

$$k_{i\to f} = \frac{2\pi}{\hbar} V_{if}^2 \rho_f \tag{2.23}$$

where V_{if} is the vibrational coupling between the initial and final state. However, the reduction of the Franck-Condon overlap integrals dominates at large energy gaps leading to a reduced rate constant. A result of the energy gap law is that, in theory, it is easier to achieve a highly emissive molecule emitting in the blue part of the radiation spectrum than in the red part [102, 103].

The intersystem crossing (ISC) is a non-radiative, isoenergetic process, where the molecules goes from the excited singlet to the excited triplet state [99]. Since the spin has to flip it is a spin-forbidden transition and thus slow. The rate constant can be increased by a stronger spin-orbit coupling allowing the transition [89, 90]. This can be achieved by introducing heavy atoms into the molecular structure. Following the energy gap law, another way to increase the ISC is to reduce the energy difference between the excited singlet and triplet state. Like IC, ISC is not reversible due to the fast vibrational relaxation. However, there are some molecules, which can undergo the reversed process after being thermally activated. Those kind of molecules exhibit then a thermally activated delayed fluorescence (TADF) [104, 105]. A requirement to show this behaviour is that the energy difference between the excited singlet and triplet states is as small as possible.

Radiative decays

A radiative decay is a process where a molecule goes from a excited state to a ground state by emitting a photon. The two main radiative decays are fluorescence and phosphorescence. The difference between these processes is that fluorescence goes from the excited singlet state to the singlet ground state, whereas phosphorescence goes from the excited triplet state to the singlet ground state. Therefore, phosphorescence is a spin-forbidden transition, which can be enhanced by spin-orbit coupling as mentioned before [89, 90]. Since the phosphorescence is a spin forbidden process its radiation lifetime is many orders of magnitudes longer than the one for fluorescence. The lifetime of radiative processes can be determined by the decrease of the emission intensity after excitation. The deactivation after excitation follows an exponential decay [106]

$$I(t) = I_0 e^{-\frac{t}{\tau}} \tag{2.24}$$

where $I(t)$ is the intensity after time t and I_0 the initial intensity when the excitation stopped. The relations between the fluorescence lifetime τ_f and the rate constants of fluorescence k_f and non-radiative processes k_{nr} is

$$\tau_f = \frac{1}{k_f + k_{nr}} \tag{2.25}$$

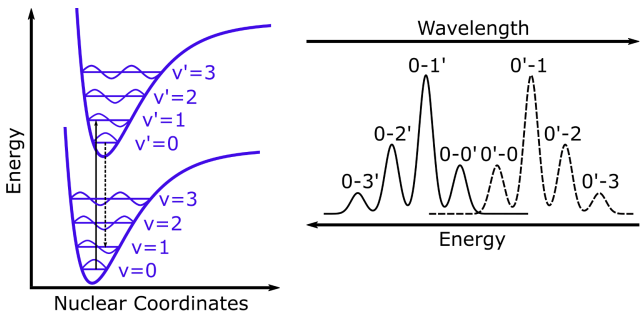

Figure 2.7: Energy scheme showing the Franck-Condon principle and the absorption (straight line) and emission (dashed line).

For the shape of the fluorescence spectrum, the Franck-Condon integrals need to be considered again [93, 94]. Due to Kasha's rule fluorescence only takes place from the lowest vibrational level of the excited state. Since the

emission process is faster than the rearrangement of the nuclei the emission behaves likes mirror-images to the absorption spectrum (Fig. 2.7). The difference between the 0-0' transition of the absorption and fluorescence of the molecule is called the Stokes shift. It normally caused by the stabilization of the excited state by the solvent. It happens because the excited state is in general more polar and more polarizable than the ground state.

Quantum yield

The fluorescence quantum yield Φ_f of a molecule is defined as the ratio between the number of emitted photons and the number of absorbed photons [107].

$$\Phi_f = \frac{number\,of\,emitted\,photons}{number\,of\,absorbed\,photons} \tag{2.26}$$

The quantum yield expresses the probability of a molecule to undergo a radiative process in contrast to the competitive processes of non-radiative decays. Following Kasha's rule the quantum yield is expected to be independent of the excitation wavelength since the process of internal relaxation is much faster than the one for the radiative and non-radiative decays. Examples for the non-radiative decays are intersystem crossing, internal conversion, external conversion and energy transfer. The quantum yield can be rewritten using the sum of the non-radiative rates k_{nr} and the radiative decay rate k_f.

$$\Phi_f = \frac{k_f}{k_f + \Sigma k_{nr}} \tag{2.27}$$

If the rate of fluorescence exceeds the rate for all non-radiative decays the quantum yield approaches unity. For higher non-radiative decays, the value approaches zero and for a molecule, which doesn't emit a photon, the quantum yield is zero. The quantum yield shows a solvent and concentration dependency according to the change of non-radiative rates. The quantum yields for other processes like IC, ISC and phosphorescence can be defined in a similar manner as ratio between their rates and all other rates.

Aggregation

In the previous sections the main focus was on the photophysical processes within one organic molecule. However, the interaction with other molecules in the surrounding needs to be considered as well to get the full, realistic picture. Organic chromophores have a tendency to stack together through strong π-π-interactions, which is caused by their structure exhibiting a rigid and planar π-core. A prominent example for aggregates are excimers, which are formed by dimerization of molecules in the excited state (Fig. 2.8). The formation of excimers leads to altered photophysical properties [108–110]. In general, a quenching of the photoluminesence and a spectral red-shift and broadening are observed. The excimer formation can be suppressed by using low concentrations since the process is concentration dependent or by introducing bulky side groups in the molecular structure, which introduces a steric hindrance for the aggregation [111–113]. Another method is the mixing of chromophores with different side chains, resulting in a stronger glass forming capability [114–116].

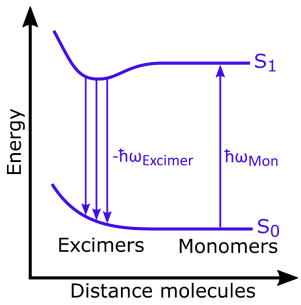

Figure 2.8: Energy scheme for the formation and emission of excimers.

Energy transfer

The energy of an excited molecule can be transferred to another molecule. The two involved molecules are normally referred to as donor and acceptor. A donor is initially in the excited state and transfers its energy to the acceptor, which becomes excited then. The energy transfer can be a radiative process, in which the acceptor is excited by an emitted photon from the donor. A requirement for this process to happen is that the emitted photon matches with the absorption spectrum of the acceptor [117].

Förster resonance energy transfer (FRET) is a non-radiative example for an energy transfer process between a donor and an acceptor [118, 119]. The energy of the donor molecule is transferred trough dipole-dipole coupling with the acceptor molecule. The rate constant of the FRET process is extremely sensitive to the distance r (to the power of six) between the donor and the acceptor and also shows a donor fluorescence lifetime τ_D dependency [120]

$$k_{FRET} = \frac{R_0^6}{r^6 \tau_D} \tag{2.28}$$

R_0 is the critical transfer distance. If the distance between the donor and acceptor is at the length of the critical transfer length, the fluorescence rate constant of the donor and the FRET rate constant are equal. Using Fermi's golden rule Eq. 2.23, Förster derived a equation for R_0 with experimentally available quantities and physical constants.

$$R_0^6 = \frac{9ln(10)}{128\pi^5 N_A} \frac{\kappa^2 \Phi_D}{n^4} J \tag{2.29}$$

where κ is the orientation factor, Φ_D is the photoluminescence quantum yield for the donor in absence of the acceptor, n is the refractive index of the medium and J is the overlap integral between the absorption of the acceptor with the emission of the donor. Due to the sensitivity towards the distance between donor and acceptor, FRET can be used as a molecular ruler, when the donor and acceptor are attached to an unknown structure. Another non-radiative process is the Dexter electron transfer [119, 121]. The difference to FRET is already obvious from the name since it is not only an exchange of energy but also of electrons. The exchange mechanism works in a way that the electron from the excited state is transferred from the donor to the acceptor and an electron from the ground state of the acceptor goes to the donor. During the exchange process the spins are conserved and both singlet-singlet and triplet-triplet energy transfers are possible. The Dexter electron transfer requires an overlap of the wavefunction of the donor and acceptor and thus is limited to very short distances.

2.3 Photochemical processes in molecules

Organic molecules cannot only undergo photophysical processes after being excited by a photon. They can also react or isomerize to other components, which is called a photochemical process. In this section photochemical processes are described in general, followed by the specific case of photoswitches and their application.

2.3.1 Photochemical reaction pathways

Chemical reactions normally occur on the potential energy surface (PES) of the ground state. Some reactions need a thermal or catalytic activation to overcome an activation energy on the reaction coordinate. In contrast to that, photochemical reactions take place after a molecule is excited by a photon to the excited potential energy surface having a significantly altered PES and therefore different reaction coordinates. Förster proposed four different photochemical reaction classes for a molecule **A** to go to product **B** with a possible intermediate state of **C** (Fig. 2.9) [120, 122].

$$A + \hbar\omega \rightarrow A^* \rightarrow \begin{cases} A^{vibr} \rightarrow B & \text{(2.30a)} \\ B^* \rightarrow B & \text{(2.30b)} \\ B & \text{(2.30c)} \\ C \rightarrow B & \text{(2.30d)} \end{cases}$$

The first class is called hot ground state reaction (Fig.2.9a). After excitation of **A**, internal conversion to a high vibrational level of the ground state occurs. Followed by vibrational relaxation into the ground state of product **B**. As a competing process also the starting molecule **A** can be obtained in the ground state. The hot reaction class works like thermally activating a reaction on the ground state to overcome an activation energy since both approaches result in a higher vibrational level. The second class is the adiabatic reaction (Fig.2.9b), where the reaction takes place on the PES of the excited state. After excitation, **A** is converted into the product **B** in the excited state, which can then go back to the ground state by emitting a photon or via IC. The third class is the diabatic reaction (Fig. 2.9c). In this case, the PESs of the ground state of **B** and the excited state of **A**

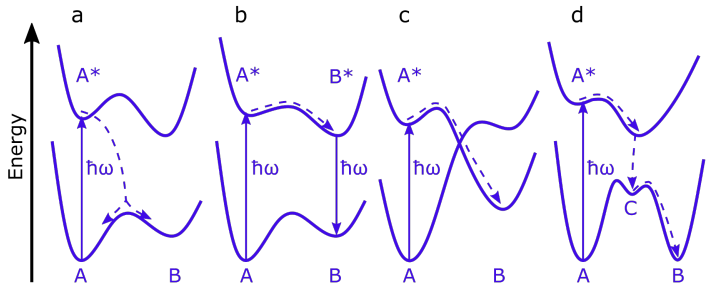

Figure 2.9: Potential energy surfaces of the ground and excited state for the classes of a) hot ground state reaction b) adiabatic reaction c) diabatic reaction and d) reaction via intermediate.

are crossing each other at the conical intersection. After exciting **A**, it can directly proceed to the photoproduct **B**. The fourth class is the reaction via an intermediate (Fig. 2.9d). The reaction proceed via a reactive intermediate and finally settles into the minimum of **B**.
For photochemical reactions, the photochemical quantum yield can be determined similar to the one for emission [123]. It is defined by the number of converted molecules divided through the number of absorbed photon by the initial molecule [107].

$$\Phi = \frac{number\,converted\,molecules}{number\,of\,absorbed\,photons} \tag{2.31}$$

Competing processes limiting the quantum yield can be all photophysical decays like IC, ISC and fluorescence. As for photophysical processes, Kasha's rule applies also for photochemical reactions, which means that all processes start from the lowest energy level of the excited state. As a consequence of that rule, the quantum yield of photochemical reactions are in general independent of the excitation wavelength.

2.3.2 Photoswitches

A special kind of photochemical reaction is the photoisomerization. During that process a molecule converts into another isomer after excitation. For photoswitchable molecules, this process is reversible by either heat

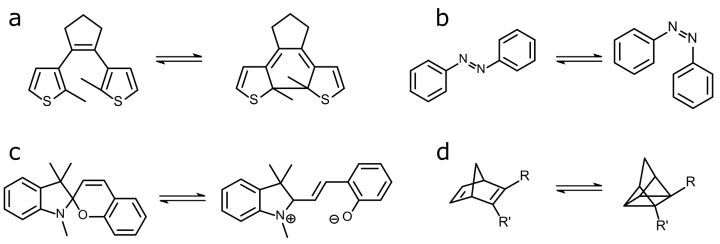

Figure 2.10: Examples for photoswitchable pairs: a) diarylethene, b) azobenzene, c) spiropyran/merocyanine and d) norbornadiene/quadricyclane.

or photoexcitation of the partner molecule. Prominent examples are diarylethene [124], azobenzene [125], spiropyran/merocyanine [126] and norbornadiene/quadricyclane [127] (Fig. 2.10). The photoisomerization quantum yield can be affected by factors like temperature, polarity of the surrounding and viscosity [123]. The impact of the factors might differ significantly, for instance, the polarity will have a major effect on the spiropyrane/merocyanine pair compared to the other pairs, which don't have any charged form.

2.3.3 Application

Photoswitches find application in molecular solar thermal energy storage systems (MOST). In those systems a photoswitch either dimerizes or isomerizes after absorbing light into a high energy metastable species (Fig. 2.11). The ground state energy differences between the two isomers is the stored energy $\Delta E_{Storage}$ of the system. The backconversion to the initial state releases the stored energy as heat. As an example, the photoswitch pair norbornadiene/quadricyclane is used in MOST [17–22]. Upon excitation norbornadiene isomerizes to quadricyclane by a [2+2] cycloaddition. The higher energy of the quadricyclane in the ground state it due to the ring strain. One of the main challenges for the use of norbornadiene is that the absorption onset is in the UV to blue area limiting the application due to their small overlap with the solar spectrum [20, 21]. Introducing electron withdrawing and electron donating groups to the structure shifts the absorption onset to higher wavelengths. However, the photoisomerization quantum yield Φ, the stored energy $\Delta E_{Storage}$ and the backconversion rate are altered at the same time. High performance devices were already achieved, but it would be

beneficial to be able to specifically engineer one characteristic of a MOST system at a time.

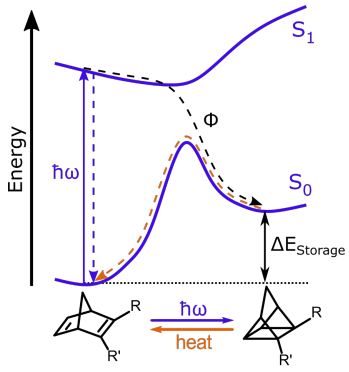

Figure 2.11: Energy scheme of a MOST system using a norbornadiene/quadricyclane photoswitch pair.

Chapter 3

Modification of excited state dynamics by the strong coupling regime

In this chapter, strong exciton-photon coupling will be described in a classical, semiclassical and full quantum picture. The characteristic behaviour of hybridization and anticrossing will be discussed as well as the strong coupling limits and the optical properties. The basic principles are followed by experimental observations on the modification of excited state dynamics in the strong coupling regime, which summarizes the work of paper **I-III**.

3.1 Principles of strong exciton-photon coupling

Classical description of strong light-matter coupling

In a classical approach light and molecular transitions can be described by harmonic oscillators. An example of a harmonic oscillator is a mass m connected to a wall by a spring with the force constant k. For the oscillation the restoring force F is defined by Hooke's law:

$$F = -kx \tag{3.1}$$

where x is the displacement of the mass from the equilibrium position. The angular frequency ω of the oscillation depends on the spring constant and

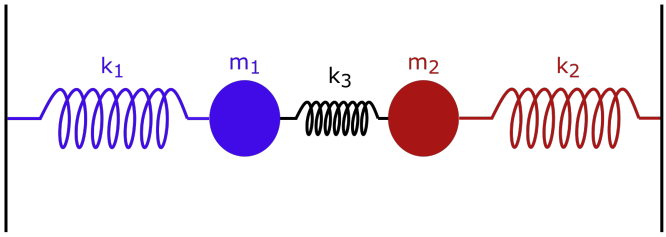

Figure 3.1: Sketch of a coupled two harmonic oscillators system.

the mass m:

$$\omega = \sqrt{\frac{k}{m}} \tag{3.2}$$

In order to model light-matter interactions, two harmonic oscillators, representing light and matter, are connected by a third spring with the spring constant k_3 (Fig. 3.1)[128]. The motion of the coupled system can be described by two equations

$$m_1 \frac{dx_1^2}{d^2t} + k_1 x_1 + k_3(x_1 - x_2) = 0 \tag{3.3a}$$

$$m_2 \frac{dx_2^2}{d^2t} + k_2 x_2 - k_3(x_1 - x_2) = 0 \tag{3.3b}$$

the labels 1 and 2 refer to the two oscillators. Solving the equations to obtain the displacement x depending on the time t, the following expressions are obtained

$$x_1(t) = Asin(\omega_+ t + C) + Bsin(\omega_- t + D) \tag{3.4a}$$

$$x_2(t) = -Asin(\omega_+ t + C) + Bsin(\omega_- t + D) \tag{3.4b}$$

where A, B, C and D are constants. The two new frequencies ω_+ and ω_- are normal modes of the system and can be determined by [128]

$$\omega_\pm^2 = \frac{1}{2}\left(\omega_1^2 + \omega_2^2 \pm \sqrt{(\omega_1^2 - \omega_2^2)^2 + 4\Gamma^2\omega_1\omega_2}\right) \tag{3.5}$$

where ω_1 and ω_2 are the frequencies of the two oscillators, which, in contrast

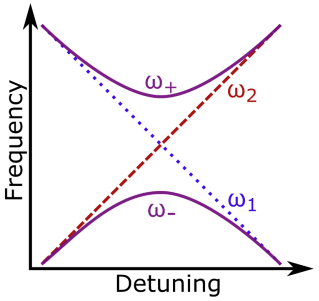

Figure 3.2: Sketch of the anticrossing behaviour of a coupled system. The detuning is the difference between the angular frequency of oscillator 1 (blue) and 2 (red).

to Eq. 3.2, also depend on the spring constant of the coupling k_3 and their frequency difference $\omega_1^2 - \omega_2^2$ is referred to as detuning

$$\omega_1 = \sqrt{\frac{k_1 + k_3}{m_1}} \; and \; \omega_2 = \sqrt{\frac{k_2 + k_3}{m_2}} \tag{3.6}$$

and the term Γ is the frequency splitting

$$\Gamma = \frac{\sqrt{k_3/m_1}\sqrt{k_3/m_2}}{\sqrt{\omega_1\omega_2}} \tag{3.7}$$

The new normal modes of the frequencies show an altered behaviour compared to the initial frequencies ω_1 and ω_2. As a consequence of Eq. 3.5, it can be seen that the frequency ω_+ is always higher than ω_-, although the initial frequencies of the separate oscillators are crossing at the point without detuning (Fig. 3.2). This behaviour is called anticrossing and it is a characteristic of the strong coupling regime. The minimum splitting is achieved for the case that the two oscillators are in resonance, meaning that they have the same frequency $\omega_1 = \omega_2$. On resonance, the splitting between ω_+ and ω_- only depends on the frequency splitting Γ and thus on the coupling strength k_3 since both are proportional to each other. With increased detuning, the splitting between the two normal modes will rise.
Another characteristic of strong coupling can be seen when rearranging Eq. 3.4 to obtain the expression for the two normal modes

$$sin(\omega_+ + C) = \frac{1}{2A}(x_1(t) - x_2(t)) \tag{3.8a}$$

$$sin(\omega_- + D) = \frac{1}{2B}(x_1(t) + x_2(t)) \tag{3.8b}$$

both normal modes depend on both positions x_1 and x_2. This means that the two oscillators cannot be treated independently anymore and can therefore be considered to be hybridized. In the analogy that the oscillators represent light and matter, hybrid light-matter states are formed as a consequence of coupling the two oscillators using a third spring.
In order to discuss the limits of the strong coupling regime, damping needs to be considered for the coupled oscillator model [128]. Therefore, the frictional terms $\gamma_1 \frac{dx_1}{dt}$ and $\gamma_2 \frac{dx_2}{dt}$ are introduced to the equation of motion Eq. 3.3. In the analogy picture of the mechanical oscillator, the friction terms represent the dissipation of the molecule and light, respectively. The strong coupling regime is achieved when the frequency splitting of the system is bigger than the dissipation in each system.

$$\frac{\Gamma}{\gamma_1/m_1 + \gamma_2/m_2} > 1 \tag{3.9}$$

Semiclassical approach

For the semiclassical approach, a quantum two level system interacting with a classical electromagnetic field is considered. The interaction can take place between the excited state of the molecule and the cavity mode. During this thesis this approach was already used, when describing the Rabi oscillation in Section 2.1.4. The Rabi frequency Ω_R as well as the detuning δ between the frequency of the molecular transition and the frequency of the light were established and will be used here again for the description of the strong coupling. Furthermore, the generalized Rabi frequency Ω can be defined depending on the Rabi frequency and the detuning.

$$\Omega = \sqrt{\delta^2 + \Omega_R^2} \tag{3.10}$$

For the quantum two level system, the ground state $|g\rangle$ and the excited state $|e\rangle$ are defined as basis vectors

$$|g\rangle = \begin{pmatrix} 0 \\ 1 \end{pmatrix} \; and \; |e\rangle = \begin{pmatrix} 1 \\ 0 \end{pmatrix} \tag{3.11}$$

For the interaction with the electric field, three different operators are introduced. The inversion operator $\hat{\sigma}_z$, the raising operator $\hat{\sigma}_+$, which brings the

two level system from its ground state to the excited state, and the lowering operator $\hat{\sigma}_-$, which brings the two level system from the excited state to the ground state. Those operators can be expressed by Pauli matrices [129]

$$\hat{\sigma}_z = \begin{pmatrix} 1 & 0 \\ 0 & -1 \end{pmatrix} \ , \ \hat{\sigma}_+ = \begin{pmatrix} 0 & 1 \\ 0 & 0 \end{pmatrix} \ and \ \hat{\sigma}_- = \begin{pmatrix} 0 & 0 \\ 1 & 0 \end{pmatrix} \tag{3.12}$$

The Hamiltonian of a coupled system is then [130]

$$\hat{H} = \frac{1}{2}E_e(\mathbf{I} + \hat{\sigma}_z) + \frac{1}{2}E_g(\mathbf{I} - \hat{\sigma}_z) + \hbar\Omega_R(\hat{\sigma}_+ + \hat{\sigma}_-)cos(\omega t) \tag{3.13}$$

where E_e and E_g is the energy of the excited and ground state, respectively, and $\mathbf{I}$ is the identity matrix

$$\mathbf{I} = \begin{pmatrix} 1 & 0 \\ 0 & 1 \end{pmatrix} \tag{3.14}$$

Using the rotating wave approximation (RWA), the Hamiltonian becomes [131]

$$\hat{H} = -\frac{\hbar\delta}{2}\hat{\sigma}_z + \frac{\hbar\Omega_R}{2}(\hat{\sigma}_+ + \hat{\sigma}_-) \tag{3.15}$$

Diagonalizing the Hamiltonian leads then to the eigenvalues of the system E_1 and E_2

$$E_1 = -\frac{1}{2}\hbar\sqrt{\delta^2 + \Omega_R^2} \tag{3.16a}$$

$$E_2 = \frac{1}{2}\hbar\sqrt{\delta^2 + \Omega_R^2} \tag{3.16b}$$

As for the normal modes in the classical picture, the two eigenstates show an anticrossing behaviour with minimal energy difference at resonance, where $\delta = 0$. For the resonance case, the splitting strength is $\hbar\Omega_R$, which is called the Rabi splitting. From the relation in Eq. 2.9, the dependence of the Rabi splitting on the transition dipole moment of the two level system $\mathbf{d}$ and the electric field amplitude $|E_0|$ can be seen.
For the eigenstates $|1\rangle$ and $|2\rangle$ the following expressions can be obtained:

$$|1\rangle = -sin(\vartheta)|e\rangle + cos(\vartheta)|g\rangle \tag{3.17a}$$

$$|2\rangle = cos(\vartheta)|e\rangle + sin(\vartheta)|g\rangle \tag{3.17b}$$

where

$$sin(\vartheta) = \frac{\Omega_R}{\sqrt{(\Omega - \delta)^2 + \Omega_R^2}} \tag{3.18a}$$

$$cos(\vartheta) = \frac{\Omega - \delta}{\sqrt{(\Omega - \delta)^2 + \Omega_R^2}} \tag{3.18b}$$

The eigenstates are hybrid states between the ground state $|g\rangle$ and the excited state $|e\rangle$. In contrast to the classical description they show a mixing parameter of $sin(\vartheta)$ and $cos(\vartheta)$, which depend on the Rabi frequency and the detuning of the samples. For the resonance condition, the contribution of both parts is 1/2. This relation changes when detuning the system. As already seen in section 2.1.4, the system oscillates between the ground and excited state when exposed to the classical electromagnetic field. When the field frequency and the transition frequency are on resonance the oscillation occurs with the Rabi frequency Ω_R for the resonance condition [132]. For detuning, the oscillation shifts to the frequency defined by the general Rabi frequency Ω.

Quantum description

For the full quantum description of light-matter interactions not only the molecular transition, described by a quantum two level system, but also the electromagnetic field inside an optical cavity is quantized (Fig. 3.3). For the two level system, the same inversion, raising and lowering operators can be used as already described in the semiclassical approach. For the quantized field, the creation operator $\hat{a}^\dagger$, which creates a photon, and the annihilation operator $\hat{a}$, which eliminates a photon are used. So, the operation combination of a raising operator for the molecule and an annihilation operator for the photon $\hat{a}\hat{\sigma}_+$ represents the absorption process, whereas emission is displayed by the inverted combination $\hat{a}^\dagger\hat{\sigma}_-$. Using the Jaynes-Cummings model and the RWA, the Hamiltonian for the interaction becomes [26]

$$\begin{aligned} \hat{H}_{JC} &= \hat{H}_{Mol} + \hat{H}_{Cav} + \hat{H}_{Int} \\ &= \frac{1}{2}\hbar\omega_{Mol}\hat{\sigma}_z + \hbar\omega_{Cav}\hat{a}^\dagger\hat{a} + \hbar g_0(\hat{a}\hat{\sigma}_+ + \hat{a}^\dagger\hat{\sigma}_-) \end{aligned} \tag{3.19}$$

where ω_{Mol} and ω_{Cav} are the frequencies for the molecular transition and the

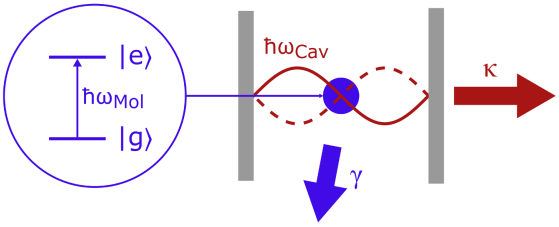

Figure 3.3: Sketch of the Jaynes-Cummings model. The molecule is represented by a two level system (blue) inside of a cavity with a cavity mode (red). The dissipation from the system are indicated by κ for the cavity photon and γ for the molecule.

cavity transition, respectively, and g_0 is the magnitude of the coupling between the molecule and the photon. The Rabi splitting $\hbar\Omega_R$ for this system is described by

$$\hbar\Omega_R = 2\hbar g_0 = 2\mathbf{d}\sqrt{\frac{\hbar\omega_{Cav}}{2\epsilon_0 V}} \tag{3.20}$$

where the square root part represents the vacuum electric field inside of a cavity E_{Cav}

$$E_{Cav} = \sqrt{\frac{\hbar\omega_{Cav}}{2\epsilon_0 V}} \tag{3.21}$$

This dependence on the electric field and transition dipole moment was already seen before in the semiclassical description of strong coupling.

By now all the descriptions of light-matter interactions only consisted of a single molecule, represented either by a harmonic oscillator or a quantum two level system. However, for the work in this thesis cavities containing a high number of molecules were used. Therefore the model needs to be extended to N quantum two level systems by using Dicke's collective operators $\hat{S}_z$, $\hat{S}_+$ and $\hat{S}_-$ [133]

$$\hat{S}_z = \sum^{N} \hat{\sigma}_z,\ \hat{S}_+ = \sum^{N} \hat{\sigma}_+ \ and\ \hat{S}_- = \sum^{N} \hat{\sigma}_- \tag{3.22}$$

Replacing the operators of the single molecule by the collective operators the Dicke Hamiltonian or also called the Tavis-Cummings Hamiltonian is obtained [134]:

$$\hat{H} = \frac{1}{2}\hbar\omega_{Mol}\hat{S}_z + \hbar\omega_{Cav}\hat{a}^\dagger\hat{a} + \hbar g_0(\hat{a}\hat{S}_+ + \hat{a}^\dagger\hat{S}_-) \tag{3.23}$$

For the case of the number of molecules N being much larger than the number of excited states, the Holstein-Primakoff transformation can be applied [135]. In this transformation the two level system operators are transformed to bosonic systems. Therefore the collective operators become

$$\hat{S}_z = \hat{b}^\dagger\hat{b} - \frac{N}{2},\ \hat{S}_+ = \hat{b}^\dagger\left(N - \hat{b}^\dagger\hat{b}\right)^{\frac{1}{2}}\ and\ \hat{S}_- = \left(N - \hat{b}^\dagger\hat{b}\right)^{\frac{1}{2}} \tag{3.24}$$

where $\hat{b}$ and $\hat{b}^\dagger$ are bosonic operators. In the large N limit, the Hamiltonian of the light-matter interaction is expressed as

$$\hat{H} \simeq \hbar\omega_{Mol}\left(-\frac{N}{2} + \hat{b}^\dagger\hat{b}\right) + \hbar\omega_{Cav}\hat{a}^\dagger\hat{a} + \hbar g_N(\hat{a}^\dagger\hat{b} + \hat{a}\hat{b}^\dagger) \tag{3.25}$$

where g_N is the magnitude of the coupling between N molecules and one photon. The Rabi splitting for the collective coupling then becomes

$$\hbar\Omega_R = 2\hbar g_N = 2\mathbf{d}\sqrt{N}\sqrt{\frac{\hbar\omega_{Cav}}{2\epsilon_0 V}} \tag{3.26}$$

which means that the coupling strength and therefore the Rabi splitting depends on the transition dipole moment of the molecule $\mathbf{d}$ and the square root of the molecular number N. In other terms the Rabi splitting is proportional to the squared root of the concentration c, which is obtained by the division of the number of molecules N through the mode volume of the cavity V.

Diagonalization of the Hamiltonian leads to the two new eigenstates, which are the upper polariton $|P^+\rangle$ and the lower polariton $|P^-\rangle$ [136] (Fig. 3.4).

$$|P^+\rangle = \alpha|e,0\rangle + \beta|g,1\rangle \tag{3.27a}$$

$$|P^-\rangle = \beta|e,0\rangle - \alpha|g,1\rangle \tag{3.27b}$$

In contrast to the semiclassical approach, the polaritonic states are not only depending on the ground $|g\rangle$ or excited $|e\rangle$ state of the two level system, but also on the Fock state of the cavity photon, where $|0\rangle$ is the absence of a cavity photon and $|1\rangle$ is the presence of a photon. The polaritons are thus hybrid states of light and matter. The contribution of the photonic or excitonic part is determined by the Hopfield coefficients $|\alpha|^2$ and $|\beta|^2$. In

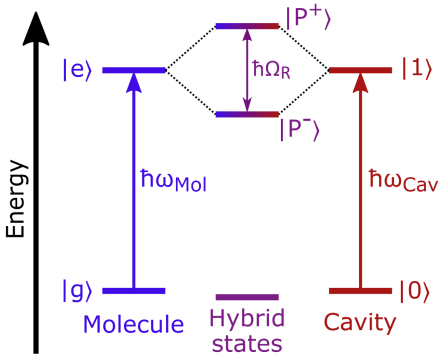

Figure 3.4: Energy diagram of the strongly coupled system showing the initial transitions of the molecule (blue) and the cavity photon (red) as well as the formed hybrid states (purple) with the Rabi splitting ($\hbar\Omega$).

case of resonance between the molecular transition and the cavity transition, both contributions are equal.

Strong coupling limits

The limits of the strong coupling regime was already discussed for the classical coupled oscillator model. In that case, the friction terms for both oscillators were introduced to describe the damping of the oscillators and the frequency splitting has to be bigger than each of the two dissipation factors. Similarly to that, dissipations for the cavity photon κ and for the molecule γ needs to be considered in the quantum picture (Fig. 3.3). Examples for those losses are photon leakage from the cavity or non-resonant relaxation of the molecule. By definition the limit of the strong light-matter coupling is that the coupling $2g$ needs to exceed the average of the two dissipation factors [137, 138]. In other words, the exchange of energy needs to be faster than the loss of the energy through dissipation.

$$2g > \frac{\gamma + \kappa}{2} \tag{3.28}$$

Experimentally, this can be observed when the absorption spectrum of the polaritons is compared with the one for the molecule and cavity mode. The strong coupling is achieved when the Rabi splitting $\hbar\Omega_R$ is larger than the full width at half maximum (FWHM) of the cavity mode (E_{Cav}) and the molecule absorption (E_{Exc}).

$$\Omega_R > \frac{FWHM(E_{Cav}) + FWHM(E_{Exc})}{2} \tag{3.29}$$

The Rabi splitting is defined as the energy difference between the upper and lower polariton when the molecular transition and cavity mode are on resonance. In case of detuning between the cavity mode and the molecular transition, the Rabi splitting can be determined by applying a coupled oscillator model on a dispersion measurement. Furthermore, a clear indicator for strong coupling is also the anticrossing behaviour in the dispersion measurement.

Coupled harmonic oscillator model

The dispersive behaviour of the polaritons is inherited by the photonic contribution, whereas the molecular transition is non-dispersive (Fig. 3.5a). The coupled harmonic oscillator (CHO) model can be used to model the dispersive experimental data to extract important parameters [139], such as the Rabi splitting $\hbar\Omega_R$ or the Hopfield coefficients $|\alpha|^2$ and $|\beta|^2$. The energy of the cavity mode in respect to the angle can be expressed as [140]

$$E_{Cav}(\theta) = E_0 \left(1 - \frac{sin^2\theta}{n_{eff}^2}\right)^{-\frac{1}{2}} \tag{3.30}$$

where E_0 is the energy of the cavity mode at normal incidence and n_{eff} is the effective refractive index. The energy can also be expressed in terms of the in-plane wavevector $k_\parallel$, which is also used quite often in the literature

$$E_{Cav}(k_\parallel) = \frac{\hbar c}{n_{eff}} \sqrt{\left(\frac{m\pi}{L_{Cav}}\right)^2 + k_\parallel^2} \tag{3.31}$$

where c is the speed of light, m is the cavity mode number and L_{Cav} is the cavity thickness. The relation between the in-plane wavevector $k_\parallel$ and the angle θ is given by

$$k_\parallel = \frac{2\pi}{\lambda} sin\theta \tag{3.32}$$

where λ is the wavelength.

For the case, that one cavity mode interacts with one exciton of a molecular transition a 2×2 matrix is used in the CHO to describe the coupling

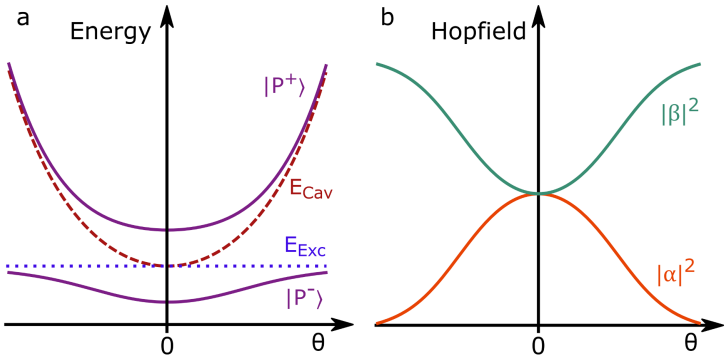

Figure 3.5: a) Dispersion of the formed polaritons (purple) at resonance of the exciton (blue) and cavity mode (red) at an angle of 0° b) Corresponding Hopfield coefficients $|\alpha|^2$ and $|\beta|^2$ to the polariton dispersion in a).

$$\begin{pmatrix} E_{Cav}(\theta) & \frac{\hbar\Omega_R}{2} \\ \frac{\hbar\Omega_R}{2} & E_{Exc} \end{pmatrix} \begin{pmatrix} \alpha \\ \beta \end{pmatrix} = E \begin{pmatrix} \alpha \\ \beta \end{pmatrix} \tag{3.33}$$

The eigenvalues of the matrix give the energy of the upper polariton E^+ and lower polariton E^-, and the eigenvectors are the Hopfield coefficients $|\alpha|^2$ and $|\beta|^2$. The energies in dependence of the angle θ can be obtained by diagonalization

$$E^{\pm}(\theta) = \frac{E_{Cav}(\theta) + E_{Exc}}{2} \pm \frac{1}{2}\sqrt{(\hbar\Omega_R)^2 + \Delta(\theta)^2} \tag{3.34}$$

where $\Delta(\theta)$ is the difference between the energy of the cavity mode E_{Cav} and the molecular transition E_{Exc}.The contribution of the photonic or excitonic part to each polariton can be determined using the following equations for the Hopfield coefficients

$$|\alpha|^2 = \frac{1}{2}\left(1 + \frac{\Delta(\theta)}{\sqrt{\Delta(\theta)^2 + 4\hbar^2 g^2}}\right) \tag{3.35}$$

$$|\beta|^2 = \frac{1}{2}\left(1 - \frac{\Delta(\theta)}{\sqrt{\Delta(\theta)^2 + 4\hbar^2 g^2}}\right) \tag{3.36}$$

For the resonance case, where the energy of the cavity mode and the energy of the molecular transition are on the same level, both parts contribute to each polariton by $\frac{1}{2}$. This contribution changes with varying the detuning

between the exciton and photon energies. From Eq. 3.31, it can be seen that the polaritons can easily be tuned between different contributions by changing the cavity thickness L_{Cav}. For thicker cavities, the energy of the cavity mode decreases. In case that the cavity energy is lower than the molecular transition, the photonic contribution to the lower polariton is increased but lowered for the upper polariton. Such systems are referred to as red-detuned. For the opposite case of blue-detuning, the energy of the cavity mode is higher than the molecular transition energy. This is easily achieved by reducing the thickness of the cavity.

Modified optical properties in the strong coupling regime

The hybrid light-matter polaritons exhibit modified optical properties compared to organic molecules, which were presented in section 2.2.3 and 2.2.4. The first striking difference are the energy levels which are higher and lower compared to the single cavity mode or the molecular transition. The Rabi splitting and thus the energy difference between the polaritons depends on the concentration and the transition dipole moment of the coupled molecule. As already discussed, polaritons show a dispersive behaviour due to their photonic contribution [141]. A characteristic of strong coupling is their anticrossing behaviour in dispersion measurements, which means that the lower polariton will only approach the excitonic energy with increasing angle. The angle-dependence is also seen for the emission of the polariton. In contrast to the absorption, the emission is normally only observed for the lower polariton. This is due to the fast relaxation of the upper polariton. Besides the two polaritons with their hybrid light-matter constitution, $N-1$ dark states are formed at the energy level of the exciton [142]. Those states have no photonic contribution and are therefore optically inactive. After exciting the upper polariton, the system relaxes down to the dark states, which are also called exciton reservoir [143]. Afterwards, the system can go to the emissive lower polariton by radiative pumping [74, 144] or vibrational-assisted relaxation [74, 145] (Fig. 3.6). In a few cases, the emission from the upper polariton was observed by thermally activating systems with a small Rabi splitting [146] or radiative pumping at low temperatures [143]. The lifetime of the strongly coupled systems will be discussed in paper **I**, which is summarized in section 3.2. The altered dynamics in the strongly coupled system in comparison to the bare molecule play a role for the interaction

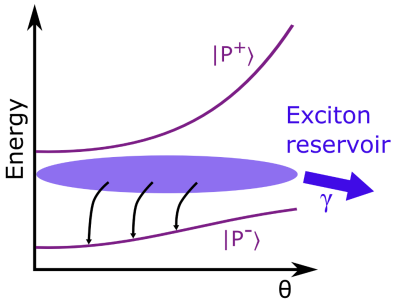

Figure 3.6: Relaxation process from the exciton reservoir to the lower polariton and the dissipation process γ for the molecule.

with other energy levels of the molecule. The photochemical reaction of photobleaching can be suppressed by strong coupling [147]. It is caused by an avoided intersystem crossing since the molecule would be bleached in its triplet state by oxygen. The efficiency of the photobleaching suppression shows a tuning dependency, where red-detuned systems have an enhanced effect of avoided ISC. The inverted process of reversed intersystem crossing is also of interest since the energy gap between the lower polariton and the molecule's triplet state can be smaller than the energy gap between the molecule's excited singlet and triplet state [148]. An increased delayed fluorescence from the lower polariton was shown for a few systems which also showed a tuning dependency [149]. Another interesting optical aspect is that due to the photonic contribution, the polaritons are delocalized over the cavity. This leads to an enhanced energy transfer distance [150–153].

The work in this thesis focuses on the excited state dynamics in the strong coupling regime. In paper **I**, the polariton lifetime and its behaviour regarding a possible angle-dependence is explored. In paper **II** and **III**, the effect of strong coupling on the photoisomerization efficiency of a photoswitch and the aggregation of molecules is discussed. All papers are summarized in the following sections.

3.2 Emission lifetime in the strong coupling regime

Hybrid light-matter polaritons exhibit a dispersive behaviour inherited by their photonic contribution. It is observed in the absorption and emission spectrum of strongly coupled systems. In paper **I**, the angle-dependent lifetime is investigated in order to see if the emission lifetime shows a dispersive character similar to the cavity photon emission. As the polaritons are described as a superposition of the photonic and excitonic contribution, a tuning dependency is also considered in this study to see whether a higher photonic contribution to the lower polariton might influence the emission lifetime.

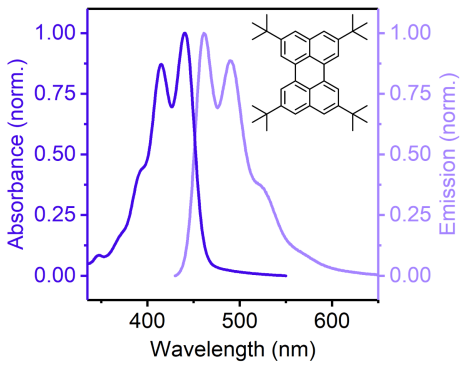

Figure 3.7: Normalized absorption (dark blue) and emission (light blue) spectrum of tetra-*tert*-butyl-perylene in a polystyrene (PS) matrix at room temperature.

The study was performed using tetra-*tert*-butyl-perylene (ttbu-perylene), which exhibits a high transition dipole moment as well as the possibility to fabricate cavities with high concentration of the molecule. This possibility is based on the molecule's high solubility and the avoided aggregation due to steric hindrance of the bulky *tert*-butyl groups. It is therefore a suitable molecule to observe strong coupling since the coupling strength depends on the transition dipole moment and the concentration as seen in Eq. 3.26.
The absorption and emission spectra of ttbu-perylene in a PS matrix (Fig. 3.7) shows a mirror image behaviour, which indicates that no aggregated states

are formed and there are no big conformational changes in the excited state. In addition, the absorption spectrum exhibits two dominant vibronic transitions and therefore the coupled harmonic oscillator model needs to be extended to a 3×3 matrix having one photonic part and two excitonic parts

$$\begin{pmatrix} E_{Cav}(\theta) & \frac{\hbar\Omega_{R,1}}{2} & \frac{\hbar\Omega_{R,2}}{2} \\ \frac{\hbar\Omega_{R,1}}{2} & E_{Exc,1} & 0 \\ \frac{\hbar\Omega_{R,2}}{2} & 0 & E_{Exc,2} \end{pmatrix} \begin{pmatrix} \alpha \\ \beta \\ \gamma \end{pmatrix} = E \begin{pmatrix} \alpha \\ \beta \\ \gamma \end{pmatrix} \tag{3.37}$$

where $E_{Cav}(\theta)$ is the energy of the cavity depending on the angle θ, $E_{Exc,1}$ and $E_{Exc,2}$ are the energy levels for the first and second vibronic transition of the molecule with the associated Rabi splittings $\hbar\Omega_{R,1}$ and $\hbar\Omega_{R,2}$, and $|\alpha|^2$, $|\beta|^2$ and $|\gamma|^2$ are the Hopfield coefficients.

The results of the CHO are displayed in figure 3.8. The transmission shows the expected dispersive behaviour for the formed lower, middle and upper polariton. Three different samples were used with altering cavity tuning. The photonic contributions to the lower polaritons are 0.60 for the rather red-detuned cavity **a** (green in figures), 0.32 for cavity **b** (orange in the figures) and 0.19 for the rather blue-detuned cavity **c** (pink in the figures). The Hopfield coefficients are changing with the angle (Fig. 3.8d-f) due to the dispersive behaviour of the cavity mode and the non-disperive of the exciton. The extracted Rabi splitting is on the same level for all three cavities. For the first excitation transition the coupling strength is around 220 meV and 180 meV for the second excitonic transition. All cavities show the strong coupling characteristic of anticrossing, which means that the polaritons approaching the energy level of the excitons but are never crossing them. Therefore, all three samples are in the strong coupling regime.

The measured emission lifetimes of the polaritons show the same emission lifetimes at all angles within the same sample (Fig. 3.9). The average lifetimes for the emission decays are determined to be 0.41, 0.46 and 0.38 ns for the cavities **a**, **b** and **c**, respectively, which indicates no substantial change by different cavity tuning. The measured emission lifetimes for the lower polariton are even exceeding the lifetime of ttbu-perylene in the PS matrix, which has an emission lifetime of 0.21 ns. The polaritonic state is a superposition of its photonic and excitonic part, hence the lifetime is expected to be determined by the fast photonic emission on a femtosecond timescale.

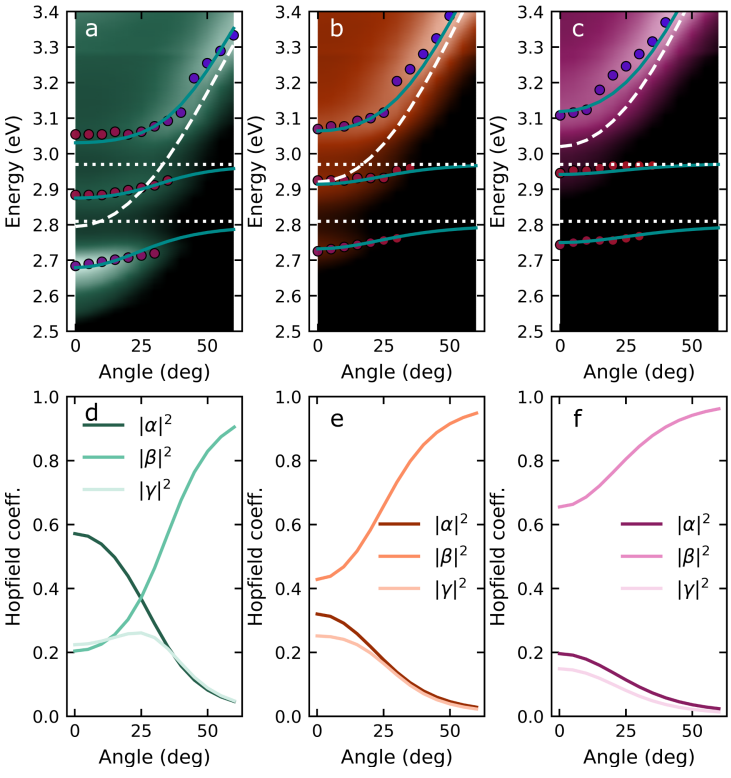

Figure 3.8: a-c) Dispersion plots of the different cavities containing ttbu-perylene in a PS matrix. The dots represent the transmission maxima of each measurement used in the coupled harmonic oscillator model (CHO) and their color represent the Hopfield coefficients ranging from blue (highly excitonic) to red (highly photonic). The teal line is the energy fit for the lower, middle and upper polariton obtained from the CHO, the dashed white line resembles the cavity energy and the white dotted line the excitonic transition for the two vibronic states. d-f) Hopfield coefficients in dependence of the angle for the three cavities obtained using the CHO.

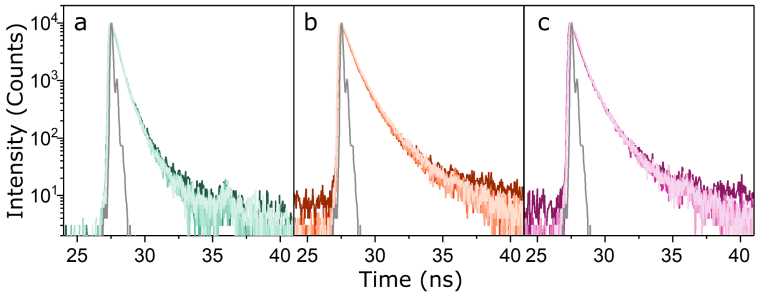

Figure 3.9: a-c) Emission lifetime measurements for the three cavities at varying angles after excitation at 405 nm. The measurements were made in 10° steps between 10° (darkest) and 60° (lightest). The gray line indicates the internal response function (IRF) of the setup.

However, the observed longer emission lifetime can be explained using the theory of the exciton reservoir. When exciting the upper polariton, like in this study, the system relaxes down to the exciton reservoir first and then to the lower polariton (Fig. 3.6). Therefore, the emission lifetime is limited by the relaxation through the exciton reservoir. This explanation is underlined by the fact that the lifetime is also tuning independent because the tuning doesn't effect the exciton reservoir.

3.3 Photoisomerization in the strong coupling regime

Strong exciton-photon coupling rearranges the potential energy surface (PES) in the excited state of molecules. In paper **II**, the impact on the photochemical properties of a photoswitch is investigated. The chosen photoswitch pair was norbornadiene/quadricyclane (NBD/QC), which finds application as a solar thermal fuel. However, the system would benefit from the possibility to adjust photochemical properties, independently.
NBD can photoisomerize to QC upon excitation. During this process the double bonds in the NBD molecule are converted into a strained four ring in QC with a higher ground state energy. The QC can convert back to the initial NBD on the ground state, releasing the excess energy as heat. The

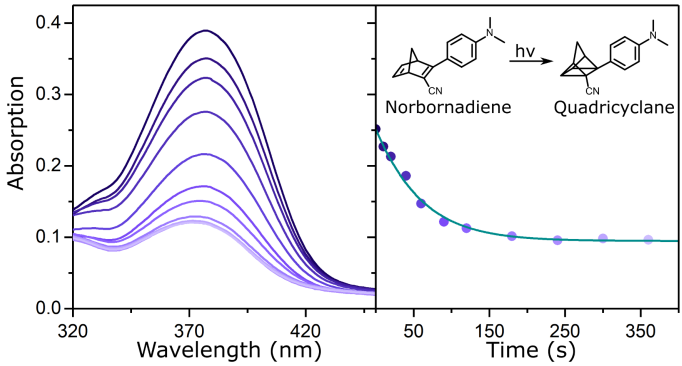

Figure 3.10: Absorption spectra of NBD in a PS after certain times of illumination at 350 nm. On the right side, the absorption decay at 350 nm over time is plotted. The teal line is the fit to determine the photoisomerization efficiency. The molecular structure of the NBD derivative photoisomerizing to the QC derivative is embedded in the figure.

structural rearrangement of the process is small and hence the photoswitch can be used in a rigid PS matrix. The photoisomerization quantum yield Φ is defined as the ratio between converted molecules and absorbed photons

$$\Phi = \frac{number\,converted\,molecules}{number\,of\,absorbed\,photons} \tag{2.31}$$

The process of photoisomerization can be followed by measuring the absorption of the sample (Fig. 3.10) at certain times. The absorption A decreases with lowering the concentration of NBD in the transparent PS matrix following Beer-Lambert's law

$$A(\lambda) = \epsilon(\lambda)cl \tag{3.38}$$

where ϵ is the molar absorptivity and l the pathlength of the sample. The change of the absorption over irradiation time $\frac{dA}{dt}$ can be used to determine the photoisomerization quantum yield Φ using the differential equation

$$\frac{dA}{dt} = -\frac{1000\,\Phi\,\epsilon\,I\,(1-10^{-A(t)})}{N_A} \tag{3.39}$$

where I is the photon flux density, t is the time of irradiation and N_A is the Avogadro constant. Fitting the measured absorption data with the differential equation (Fig. 3.10), the photoisomerization quantum yield of NBD is

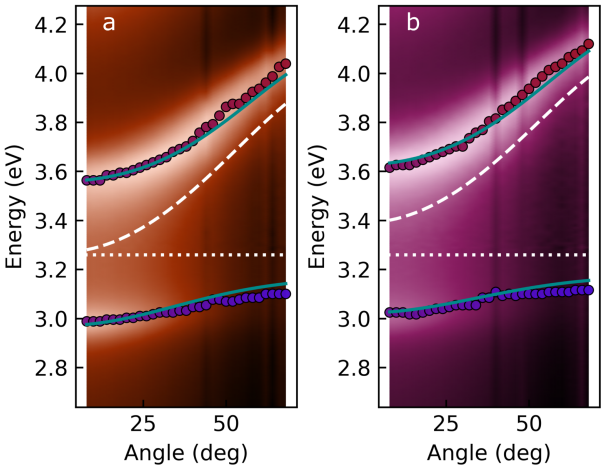

Figure 3.11: Dispersion plots of the different cavities containing NBD in a PS matrix. The dots represent the reflectance maxima of each measurement used in the coupled harmonic oscillator model (CHO). The teal line is the energy fit for the lower and upper polariton obtained from the CHO, the dashed white line shows the cavity energy and the white dotted line the excitonic transition.

determined to be 95% in a PS matrix. The backconversion half-life, when 50% of the molecules are converted back to the initial NBD form, is estimated to be 5.9±0.8 days.

Two samples with different cavity tuning were prepared to study the impact of the strong coupling regime on the photoisomerization quantum yield. The dispersion plots of the two cavities are displayed in Fig. 3.11. Applying the coupled harmonic oscillator model to the dispersion, the Rabi splitting and the Hopfield coefficients were extracted. For the tuned cavity **a**, the photonic contribution to the lower polariton is 0.47 and the Rabi splitting is 589 meV. For the blue-detuned cavity **b**, the photonic contribution is 0.38 and the Rabi splitting is 591 meV. Since the Rabi splitting of both cavities is bigger than the FWHM of the molecular transition (530 meV) and the cavity resonance (390 meV), both samples are in the strong coupling regime. The photoisomerization quantum yield of both samples are determined for excitation at the upper polariton, lower polariton and at the transition maximum of NBD. In contrast to the molecule in the film a different attempt is used to determine the photoisomerization quantum yield in the

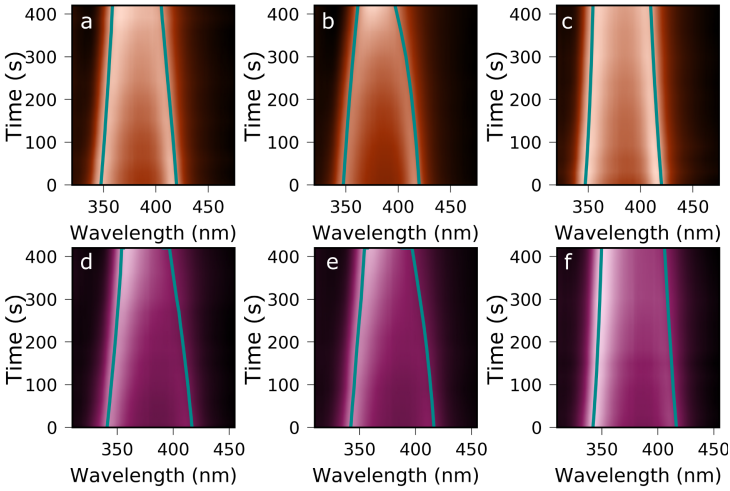

Figure 3.12: Photoisomerization progress over time for the tuned cavity (orange) for an excitation at a) 350 nm, b) 380 nm and c) 415 and for the blue-detuned cavity (pink) for an excitation at d) 345 nm, e) 380 nm and f) 410nm.

strong coupling regime. This is necessary because the Beer-Lambert's law doesn't apply for the hybrid polaritons. The shape of their spectrum mainly depends on the Rabi splitting and the photonic contribution to each polariton. The relation that the splitting strength is proportional to the squared root of the number of molecules (Eq 3.26) was used to determine the photoisomerization quantum yield. The change of the splitting over time for all measurements are displayed in Fig. 3.12.

The photoisomerization quantum yield of the measurements was displayed in Fig. 3.13. It is calculated by the ratio between the absorbed photons, obtained by the reflectance of each sample at the excitation wavelength, and the converted molecules, obtained by the change of the splitting. For excitation at the upper polariton and at the molecular transition maximum, the photoisomerization quantum yield is in the range of 70-90% for both samples, which is comparable to the molecular photoisomerization efficiency (95%). However, the photoisomerization efficiency drops significantly for the excitation at the lower polariton. This finding can be explained by the arising competing processes of cavity photon emission and population of the exciton reservoir from the lower polariton, when it is excited. Exciting the

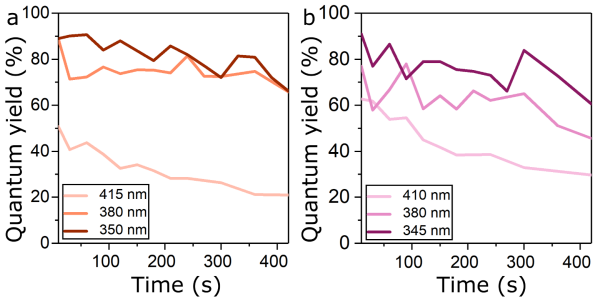

Figure 3.13: Calculated quantum yields for the tuned cavity (orange) and the blue-detuned cavity (pink) after different excitation times at varying excitation wavelength.

upper polariton, the process of vibration-assisted population of the exciton reservoir is energetically allowed and therefore the photoisomerization quantum yield is unperturbed. This explanation is underlined by the fact, that the observed reduction is pronounced for the sample, which has a higher photonic contribution and lower energy level of the lower polariton. In that case, the fast process of the cavity photon emission is more dominant since the overlap between the exciton reservoir and the lower polariton is reduced and therefore less transfer from the lower polariton to the exciton reservoir occurs.

3.4 Changed aggregation properties

Similarly to the photoisomerization process, the formation of excimer occurs when a molecule is in its excited state (Fig. 2.8). Therefore, the aggregation dynamics of molecules in the strong coupling regime are investigated paper **III**.

Two different molecules are used in this study; both having a different way of forming aggregated states. The first molecule is 1-ethyl-perylene (et-perylene), which has similar properties like ttbu-perylene in as described section 3.2. However, et-perylene shows a broad structureless excimer emission having a maximum at 520 nm (Fig. 3.14a). The second molecule is DABNA-2, which shows two narrow peaks for absorption and prompt emission at 448 nm and 490 nm, respectively (Fig 3.14b). Additionally, the molecule can undergo thermally activated delayed fluorescence (TADF) due

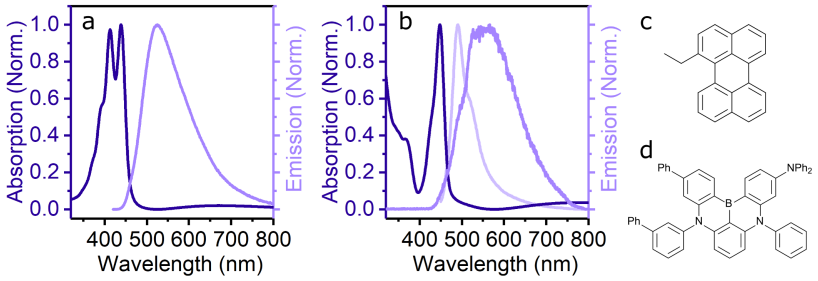

Figure 3.14: a) Normalized absorption (dark blue) and emission (blue) spectrum of the 1-ethyl-perylene in a polystyrene matrix. Also showing the molecular structure. b) Normalized absorption (dark blue), delayed fluorescence (blue) and prompt fluorescence (light blue) spectrum of a pristine DABNA-2 film. c) Structure of 1-ethyl-perylene and d) structure of DABNA-2.

to the low energy difference between the triplet and singlet excited state. The delayed fluorescence shows a broad structureless excimer emission with a maximum around 600 nm. The reason why the excimer emission is present in the delayed fluorescence but not in the prompt emission can be explained by the longer lifetime of the triplet state. The molecule can form the aggregate in the triplet state and the RISC takes place between the aggregated triplet manifold and the aggregated singlet manifold.

For both molecules different cavities with different tunings are investigated. The rough tuning of the cavities are indicated in Fig. 3.15e. For et-perylene, four different samples are presented. The photonic contributions to the lower polariton are ranging from 0.64 for the most red-detuned cavity over 0.50 and 0.36 to 0.22 for the most blue-detuned cavity (Fig. 3.15a-d). The Rabi splittings are all in the same range of 332-348 meV for the first transition and 370-384 meV for the second transition. They are bigger than the estimated FWHM of the corresponding transitions, which are 140 meV for the first and 196 meV for the second transition. The values are all extracted from a coupled harmonic oscillator model using a 3×3 matrix. For DABNA-2, two different samples are prepared (Fig. 3.15f,g). A rather red-detuned sample with a photonic contribution to the lower polariton of 0.62 and a rather blue-detuned one with a contribution of 0.42. The Rabi splitting of both cavities are around 400-420 meV and therefore larger than the FWHM of the molecular transition, which is 190 meV. The values are obtained using

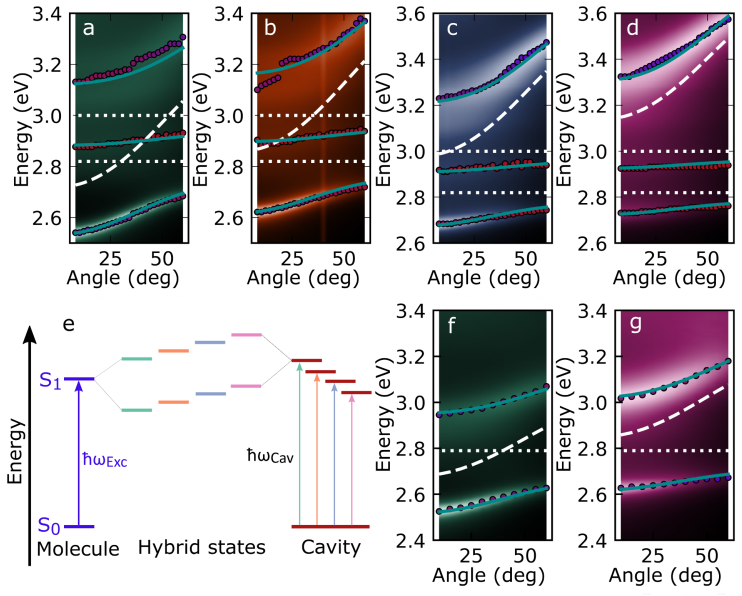

Figure 3.15: Dispersion plots of the different cavities containing a-d) et-perylene in a PS matrix and f,g) DABNA-2. The dots represent the reflectance maxima of each measurement used in the coupled harmonic oscillator model (CHO). The teal line is the energy fit for the lower and upper polariton obtained from the CHO, the dashed white line shows the cavity energy and the white dotted line the excitonic transition. e) Indicating the energy level in the differently tuned cavities.

a two harmonic oscillator model. All cavities show the characteristic anti-crossing behaviour and their Rabi splitting is bigger than the FWHM of the corresponding transition, therefore all samples are in the strong coupling regime.

Measuring the optical properties of the strongly coupled et-perylene, the emission spectra show a clear tuning dependency (Fig. 3.16a). The polariton emission and the excimer emission show two opposite trends. The highest polaritonic emission is measured for the most red-detuned, gradually decreasing to the blue-detuned cavity. This trend is vice versa for the excimer emission. Since the mirror thicknesses are the same for all sample, the reason for the observation is not the quality factor but the different tuning of the cavities. The emission spectra are obtained from the excitation of the upper polariton. To get a deeper understanding how the excimer states are popu-

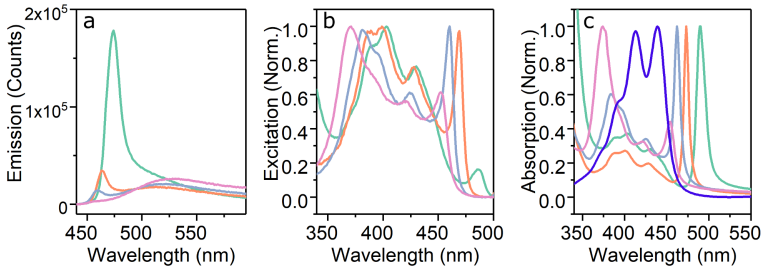

Figure 3.16: a) Emission spectra of the four differently tuned cavities containing et-perylene. b) Normalized excitation spectra for the four cavities for the emission at 520 nm. c) Comparison of the absorption of the four cavities with the bare film absorption of et-perylene in a PS matrix.

lated, excitation spectra for the emission at 520 nm are made (Fig. 3.16b). It is striking that there is almost no excimer emission for the excitation of the lower polariton for the most red-detuned cavity. There is also a mismatch between the absorption (Fig. 3.16c) and the excitation spectrum for all samples. The mismatch is the biggest for the most red-detuned cavity and gradually decreases to the most blue-detuned cavity. Similar to the photoswitch, those findings can be explained by a competing process between the polariton emission and the formation of the aggregated states, which can either occur directly or via the exciton reservoir. For the most red-detuned cavity, the energy level of the lower polariton is the lowest for all samples. With decreasing energy level of the lower polariton, the overlap with the exciton reservoir, whose density of state is essentially that of the molecule, is reduced or even removed like for the presented red-detuned cavity. Therefore, it is energetically unfavourable to populate the exciton reservoir. Furthermore, the direct transition to the excimer can be reduced since the driving force is minimized due to the change in the energy levels. With increasing blue-detuning, the overlap and the energy level of the polariton increases and accordingly the excimer emission.

Turning the attention to the cavities containing DABNA-2, the delayed emission of the samples show a similar tuning dependency as the previous case of prompt emission. The rather blue-detuned cavity shows a higher excimer emission and the rather red-detuned cavity shows a higher polaritonic emission. However, the excimers are formed in the triplet manifold and thus it cannot be argued that their formation is avoided like in the case for

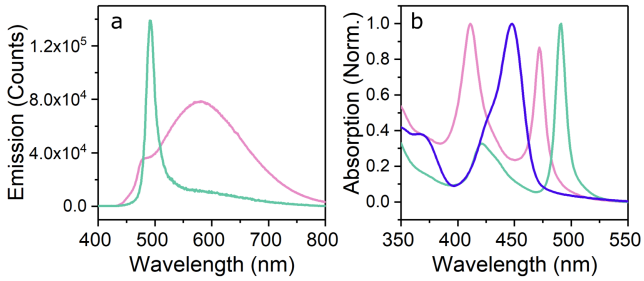

Figure 3.17: a) Emission spectra of the two differently tuned cavities containing a pristine film of DABNA-2. b) Absorption comparison between the bare film of DABNA-2 (blue) and the two cavities.

et-perylene. The red-detuned cavity shows almost exclusively delayed polaritonic emission (Fig. 3.17a), hence a direct excimer to polariton transition needs to occur. In contrast to the blue-detuned cavity, the lower polariton of the red-detuned cavity lies energetically below the exciton reservoir, which reduces possible transitions between those two states. Additionally, the energies of the polariton and the excimer state are quite similar, which further increases the driving force towards the polaritonic state for decreasing energy levels of the lower polariton. As seen before, the radiative decay is fast once the lower polariton is reached. So all in all, it is shown that the excimer emission can be controlled by changing the tuning of strongly coupled systems. This behaviour is seen in both prompt and delayed emission but their dynamics might differ. The formation is avoided in the prompt emission case, whereas a direct excimer to polariton transition is present in the delayed emission case.

Chapter 4

Methods

In this chapter, the methods of sample preparation and optical characterization are presented. The thin layer deposition methods magnetron sputtering and spincoating are presented in the first two sections. They were used to prepare the optical cavities containing a chromophore in a polymer matrix. The section is followed by the description of ultraviolet-visible spectroscopy, steady-state photoluminescence and time correlated single photon counting, which were the used techniques to analyze the samples.

4.1 Magnetron sputterer

Magnetron sputtering is a physical vapour deposition (PVD) method to deposit thin films on a substrate [154]. High voltage (∼500V) is applied to generate a plasma between the cathode and the anode. The role of the magnets in the magnetron sputtering source is to confine the electrons close to the surface of the target leading to a higher plasma density and an increased deposition rate.
During the sputtering process the vacuum chamber is first evacuated to remove all contaminating gases and to reduce the partial pressure of all background gases. The inert gas Argon is then injected and gets positively charged in the plasma, and is accelerated towards the negatively charged cathode located below the target. The kinetic energy of the impact is high enough to eject atoms from the metallic target. The loose atoms travel through the high vacuum chamber and are deposited on the substrate and walls (Fig. 4.1). The thickness of the deposited film is controlled by a quartz

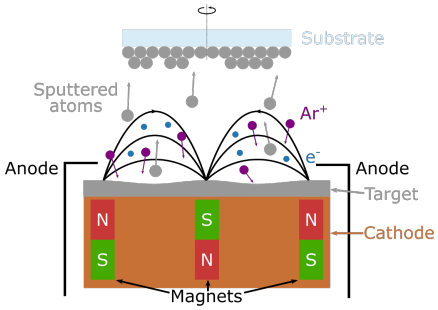

Figure 4.1: Sketch of the magnetron sputtering process.

crystal microbalance (QCM), which is located close to the substrate holder. The frequency of the piezoelectrical quartz crystal is affected by the deposition on the surface of the crystal. The thickness can be controlled on a subnanometer scale.
Magnetron sputtering was used to deposit silver or aluminium mirrors in order to prepare the optical cavities in paper **I-III**. The choice of metal was based on the reflectivity of the metal at the wavelength of molecular absorption.

4.2 Spincoating

Spincoating is a fairly simple but powerful technique to prepare uniform solid films of organic molecules. Before spincoating, the molecule is dissolved in a suitable solvent. This solution is dropped onto a substrate in the spincoater. Then the rotation is started and accelerated to the desired rotational speed. Most of the solution is expelled due to centrifugal forces. Under rotation, the viscous film starts to thin and the rest of the solvent is evaporated by an air flow resulting in a solid film of the molecule. The thickness of organic films can be adjusted by varying the concentration of the spincoated solution, the solvent or the rotational speed during the spincoating process. A thicker film is achieved by either a higher concentration or a lower rotational speed.
The spincoating technique was used in paper **I-III** to prepare the optical active layer inside the optical cavity. Therefore, the dye molecule and polystyrene were dissolved in a desired mass ratio in a suitable solvent. The

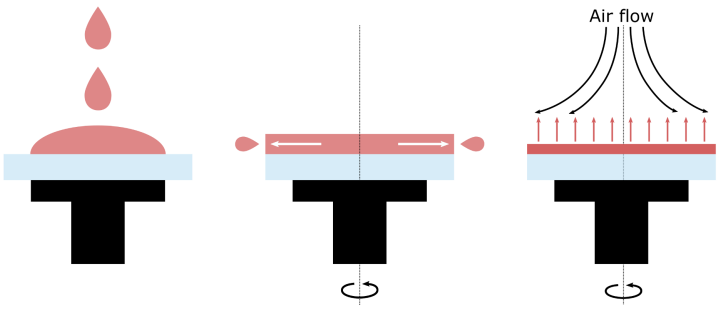

Figure 4.2: Sketch of the spincoating process.

overall concentration of both molecules were used to get the right thickness to couple to one of the cavity modes; normally the lambda mode was used. The fine-tuning was done by changing the rotational speed during the spincoating process making it possible to produce cavities with different detuning of the strong exciton-photon coupling.

4.3 Ultraviolet-visible spectroscopy

Ultraviolet-visible spectroscopy (UV-Vis) is a technique to measure the electronic and vibronic transitions of a molecule. It gives an insight on the molecule's singlet energy levels and how strongly they interact with light. The absorption depends on the molecule's molar absorptivity ϵ, which is specific for a molecule and wavelength dependent. The absorption at a certain wavelength $A(\lambda)$ is described by the Beer-Lambert-Bouguer law

$$A(\lambda) = \epsilon(\lambda)cl \tag{4.1}$$

where c is the concentration of the sample and l the path length of the sample, which is passed by the light.
A typical set-up is the double beam UV-Vis spectrophotometer (Figure 4.3). In this setup, the light of a lamp with a broad spectrum is monochromated and split up into two different beams. One beam passes through the sample and the other passes through a reference sample. In the end both light beams are detected and the absorption $A(\lambda)$ is determined by the following equation:

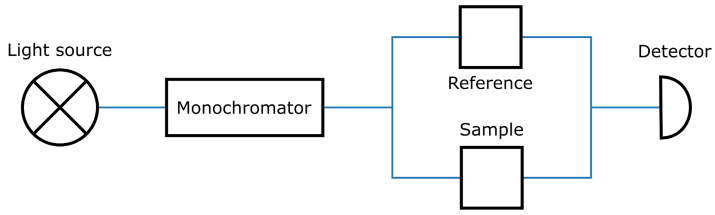

Figure 4.3: Sketch of a dual beam UV-Vis spectrophotometer setup.

$$A(\lambda) = log\frac{I_0(\lambda)}{I(\lambda)} \tag{4.2}$$

where $I_0(\lambda)$ is the intensity of the transmitted light of the reference beam and $I(\lambda)$ the intensity of the transmitted light through the sample. The reference sample is the solvent in a cuvette for liquid samples or the substrate for solid state samples.
The UV-Vis spectrophotometer can also measure the reflectance with a reflective sample holder. The reference sample in that case is a mirror with known reflectance. The relation between absorption $A\%(\lambda)$, transmittance $T\%(\lambda)$ and reflectance $R\%(\lambda)$ is

$$A\%(\lambda) = 100\% - R\%(\lambda) - T\%(\lambda) \tag{4.3}$$

For a reflective sample without any transmittance $T\%(\lambda) = 0$, the absorption $A\%(\lambda)$ of the sample can be directly calculated from the reflectance $R\%(\lambda)$.
In paper **I-III**, the UV-Vis spectrophotometer was used to detect the peak position of the upper and lower polariton. A coupled harmonic oscillator model was used to fit the dispersive behaviour of the polaritons in order to receive the Rabi splitting $\hbar\Omega_R$ and the Hopfield coefficients of the different samples. Additionally, the absorption of the samples in paper **II** were measured to follow the photoisomerization process and to be able to calculate the photoisomerization efficiency.

4.4 Steady-state photoluminescence

A spectrofluorometer can be used to study the emission properties of a sample [106]. The setup can be divided up into an excitation arm and an emission arm. The excitation arm consists of a light source with an broad spectrum such as a xenon lamp, and a monochromator. The monochromated light excites the sample and the emitted light is measured in the emission arm located in an angle of 90 degree to the excitation arm. The light beam passes through a monochromator before it is measured by a detector. For highly scattering or absorbing samples a front face mode using mirror optics can be used to measure the emission coming from the part of the sample where the excitation beam hits it first. Two different modes can be run to measure either the excitation or emission spectrum of a compound. For the emission spectrum, the excitation wavelength is fixed and the emission is measured for different wavelengths. For the excitation spectrum, the emission wavelength is fixed and the excitation wavelength varies. In general, a low absorption of the sample is required to avoid inner filter effects. Samples with a small Stoke's shift and high absorption can reabsorbed the emitted light and therefore manipulate the measured emission spectrum. Another effect of highly absorbing samples is that the excitation light has already a lower intensity at the point from where the emission is measured because it was absorbed by the sample before that point.
Polaritons inherit the optical dispersive behaviour from the photonic contribution making it crucial to measure an angle-resolved emission spectrum for strongly coupled samples [141]. This is not possible with the previously described setup since the angle between the excitation and emission arm is fixed. To measure an angle-resolved emission spectrum a mirror is placed at the position of the sample reflecting the excitation light into an optical light fiber. At the end of that optical light fiber the excitation light is collimated onto the sample. The emitted light is then collected by another fiber at an adjustable angle between 0 and 60 degree. The light is guided back into the spectrofluorometer where it is measured by the detector after passing through the monochromator (Fig. 4.4).
In paper **I** and **III**, the emission of the bare films were measured using the spectroflourormeter if not stated differently. However, the emission of the strongly-coupled systems were determined using the angle-resolved setup.

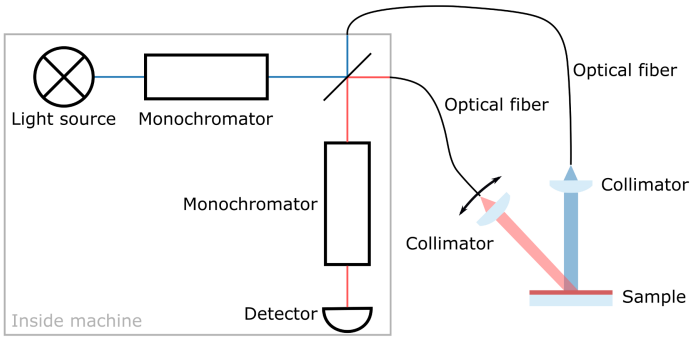

Figure 4.4: Sketch of the spectrofluorometer connected via optical fibres to the homemade setup measuring the angle-dependent steady-state photoluminescence

4.5 Time-correlated single photon counting (TCSPC)

In general, molecules can relax down from the excited state to the ground state by different radiative and non-radiative decays. The relaxation of simultaneously excited molecules does not take place at the same time since the relaxation is based on probability. The reduction in emission intensity I is described by equation 2.24 [106].

$$I(t) = I_0 e^{-\frac{t}{\tau}} \tag{2.24}$$

where I_0 is the initial intensity, t is the time and τ is the emission lifetime of the molecule. The emission lifetime τ of an organic molecule can be measured using the time-correlated single photon counting technique. During that measurement, the sample is excited by a short pulsed laser, which also starts a timer. The detection of an emitted photon stops the timer (Fig.4.5a and b). This process is repeated until a statistically significant number of measurements are done. All the measured times are plotted in a histogram against the number of counts (Figure 4.5c). Since only the first photon is detected it is crucial that less than one photon is collected per 100 excitation pulses [106]. Otherwise there is the chance that two photons are emitted

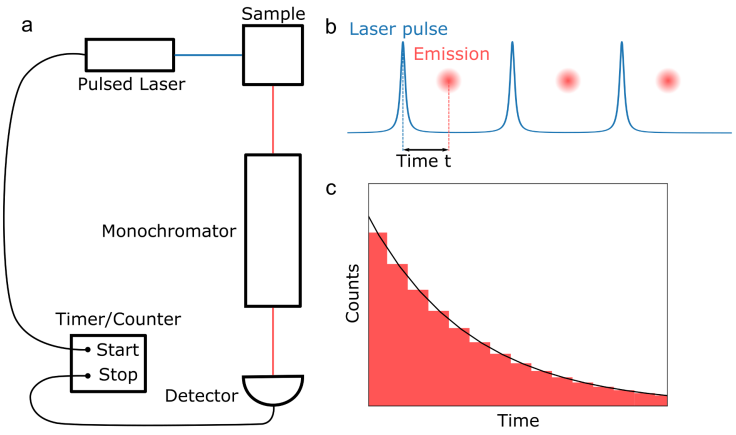

Figure 4.5: a) Sketch of the TCSPC setup to measure the time-resolved photoluminescence b) measurement of start-stop times with TCSPC and c) histogram of the measured times.

and the measurement can be shifted to a shorter lifetime. The decay of the histogram resembling the intensity decay at a certain emission wavelength can be fitted using equation 4.4.

$$I(t) = \sum_{i=1}^{n} \alpha_i e^{-\frac{t}{\tau_i}} \tag{4.4}$$

It can be described as a sum of different emitting components at a certain wavelength. The pre-exponential factor α_i represents the amplitude of a component at the time $t = 0$. τ_i is the decay time of the component and n is the number of components. The different components of a multi-exponential decay can be the result of a mix between different chromophores emitting light at the same wavelength with different decays or different regions of a sample having differing morphology or aggregational states.
The resolution of the measurements depend on the pulse width of the excitation laser and on the response time of the detector. The laser width and detector response are measured as instrument response function (IRF), and involved in the fitting of the reconvolution fit.
TCSPC was used to determine the emission lifetime of polaritons and molecular films in paper **I** and **III**. Additionally, the angle-resolved lifetime was measured for paper **I**.

Chapter 5

Summary and Outlook

The work in this thesis focused on the excited state dynamics of strongly coupled systems. The studies were performed using organic molecules which were embedded in an optical cavity.
In the study of paper **I**, tetra-*tert*-butyl perylene was strongly coupled to a cavity mode. Using optical spectroscopy, the emission lifetime was measured depending on the emission angle and on the tuning of different cavities. In both cases, the systems didn't show any dependency, which was concluded to be due to the exciton reservoir. After excitation of the upper polariton, the system relaxes quite fast to the exciton reservoir, which are optically inactive states at the energy of the molecular transition. Those states have no photonic contribution and therefore they are non-dispersive. The angle-independent emission lifetime is the consequence of the relaxation through those states limiting the emission lifetime to the timescale of a bare molecule.
In paper **II**, the effect of strong coupling on the photoisomerization quantum yield of the photoswitch NBD was studied. The results showed a clear dependency on whether the system is excited at the upper or lower polariton. For the excitation of the upper polariton and the transition maximum of the molecule, the photoisomerization quantum yield was on the same level as for the bare molecule. However, the quantum yield decreases significantly when exciting the lower polariton. This observation was explained by the competing processes of cavity photon emission and populating the exciton reservoir from where the molecule can undergo the photoisomerization process. For excitation at the upper polariton or the molecular transition, the

system relaxes quite fast to the exciton reservoir, which was already discussed in paper **I**. For the excitation at the lower polariton, the process of populating the exciton reservoir is energetically unfavourable leading to a decreased photoisomerization quantum yield. This picture is supported by the observed tuning dependency. The effect of a lowered photoisomerization quantum yield is emphasized for the cavity with a higher photonic contribution and lower polariton energy level.
For the final paper **III**, the interplay between the excited states of strongly coupled systems and aggregated trap states of the molecule was explored. In a first approach, 1-ethyl-perylene was used, which shows prompt excimer emission in a bare film. The emission of strongly coupled samples of 1-ethyl-perylene showed a clear tuning dependency. The more red-detuned the cavities were, the stronger was the polariton emission. However, for the blue-detuned cavities the excimer emission increased. It can be explained by the decreased energy level of the lower polariton for red-detuned cavities, which can either avoid excimer formation due to a lower population of the exciton reservoir or has a increased direct transition from the excimer. In a second approach, DABNA-2 was used, which shows delayed excimer emission, which means that the aggregation takes place on the triplet manifold. For those samples, the same tuning dependency was observed. Since the excimer is formed before the polariton or exciton reservoir is populated, a direct excimer to polariton event is evident from the red-detuned cavity.
In conclusion, the excited state dynamics of strongly coupled systems were investigated here. The exciton reservoir shows to play an important role throughout all the investigations. It limits the emission lifetime and leads to the photoisomerization of photoswitches when populated. A direct transition between excimer states and polaritons are also possible. Understanding the dynamics in the excited state can be beneficial for applications such as lasing, OLED, TTA upconversion or singlet fission. As seen for paper **III**, simple changes like the tuning of a cavity can lead to a close to monochromatic emission with a high intensity. Furthermore, the knowledge about the dynamics can unveil the full potential of polaritonic chemistry. It can guide the field of strong exciton-photon coupling to a more application based research, which is already done here for the use of a solar fuel in paper **II**.

Bibliography

[1] Mony, J.; Hertzog, M.; Kushwaha, K.; Börjesson, K. *The Journal of Physical Chemistry C* **2018**, *122*, 24917–24923.

[2] Mony, J.; Climent, C.; Petersen, A. U.; Moth-Poulsen, K.; Feist, J.; Börjesson, K. *Advanced Functional Materials* **2021**, *31*, 2010737.

[3] Hertzog, M.; Wang, M.; Mony, J.; Börjesson, K. *Chem. Soc. Rev.* **2019**, *48*, 937–961.

[4] Schäfer, C.; Mony, J.; Olsson, T.; Börjesson, K. *Chemistry – A European Journal* **2020**, *26*, 14295–14299.

[5] Gutzeit, V. A.; Acosta-Ruiz, A.; Munguba, H.; Häfner, S.; Landra-Willm, A.; Mathes, B.; Mony, J.; Yarotski, D.; Börjesson, K.; Liston, C.; Sandoz, G.; Levitz, J.; Broichhagen, J. *Cell Chemical Biology* **2021**, *28*, 1648–1663.e16.

[6] Einstein, A. *Annalen der Physik* **1905**, *322*, 132–148.

[7] Bohr, N. *The London, Edinburgh, and Dublin Philosophical Magazine and Journal of Science* **1913**, *26*, 476–502.

[8] Heisenberg, W. *Zeitschrift für Physik* **1925**, *33*, 879–893.

[9] Millikan, R. A. *Phys. Rev.* **1916**, *7*, 355–388.

[10] Planck, M. *Annalen der Physik* **1901**, *309*, 553–563.

[11] Einstein, A. *Deutsche Physikalische Gesellschaft* **1916**, *18*, 318–323.

[12] Dirac, P. A. M.; Bohr, N. H. D. *Proceedings of the Royal Society of London. Series A, Containing Papers of a Mathematical and Physical Character* **1927**, *114*, 243–265.

[13] Snaith, H. J.; Schmidt-Mende, L.; Grätzel, M.; Chiesa, M. *Phys. Rev. B* **2006**, *74*, 045306.

[14] Nayak, P. K.; Mahesh, S.; Snaith, H. J.; Cahen, D. *Nature Reviews Materials* **2019**, *4*, 269–285.

[15] Kim, J. Y.; Lee, J.-W.; Jung, H. S.; Shin, H.; Park, N.-G. *Chemical Reviews* **2020**, *120*, 7867–7918.

[16] Kore, B. P.; Zhang, W.; Hoogendoorn, B. W.; Safdari, M.; Gardner, J. M. *Communications Materials* **2021**, *2*, 100.

[17] Dreos, A.; Wang, Z.; Tebikachew, B. E.; Moth-Poulsen, K.; Andréasson, J. *The Journal of Physical Chemistry Letters* **2018**, *9*, 6174–6178.

[18] Jevric, M.; Petersen, A. U.; Mansø, M.; Kumar Singh, S.; Wang, Z.; Dreos, A.; Sumby, C.; Nielsen, M. B.; Börjesson, K.; Erhart, P.; Moth-Poulsen, K. *Chemistry – A European Journal* **2018**, *24*, 12767–12772.

[19] Jorner, K.; Dreos, A.; Emanuelsson, R.; El Bakouri, O.; Fdez. Galván, I.; Börjesson, K.; Feixas, F.; Lindh, R.; Zietz, B.; Moth-Poulsen, K.; Ottosson, H. *Journal of Materials Chemistry A* **2017**, *5*, 12369–12378.

[20] Kuisma, M. J.; Lundin, A. M.; Moth-Poulsen, K.; Hyldgaard, P.; Erhart, P. *The Journal of Physical Chemistry C* **2016**, *120*, 3635–3645.

[21] Li, H. B.; Tebikachew, B. E.; Wiberg, C.; Moth-Poulsen, K.; Hihath, J. *Angewandte Chemie International Edition* **2020**, *59*, 11641–11646.

[22] Orrego-Hernández, J.; Dreos, A.; Moth-Poulsen, K. *Accounts of Chemical Research* **2020**, *53*, 1478–1487.

[23] McConnell, I.; Li, G.; Brudvig, G. W. *Chemistry & Biology* **2010**, *17*, 434–447.

[24] Gueret, R.; Poulard, L.; Oshinowo, M.; Chauvin, J.; Dahmane, M.; Dupeyre, G.; Lainé, P. P.; Fortage, J.; Collomb, M.-N. *ACS Catalysis* **2018**, *8*, 3792–3802.

[25] Ye, C.; Li, J.-X.; Li, Z.-J.; Li, X.-B.; Fan, X.-B.; Zhang, L.-P.; Chen, B.; Tung, C.-H.; Wu, L.-Z. *ACS Catalysis* **2015**, *5*, 6973–6979.

[26] Jaynes, E.; Cummings, F. *Proceedings of the IEEE* **1963**, *51*, 89–109.

[27] Yakovlev, V. A.; Nazin, V. G.; Zhizhin, G. N. *Optics Communications* **1975**, *15*, 293–295.

[28] Kaluzny, Y.; Goy, P.; Gross, M.; Raimond, J. M.; Haroche, S. *Phys. Rev. Lett.* **1983**, *51*, 1175–1178.

[29] Raizen, M. G.; Thompson, R. J.; Brecha, R. J.; Kimble, H. J.; Carmichael, H. J. *Phys. Rev. Lett.* **1989**, *63*, 240–243.

[30] Haroche, S.; Kleppner, D. *Physics Today* **1989**, *42*, 24–30.

[31] Thompson, R. J.; Rempe, G.; Kimble, H. J. *Phys. Rev. Lett.* **1992**, *68*, 1132–1135.

[32] Weisbuch, C.; Nishioka, M.; Ishikawa, A.; Arakawa, Y. *Phys. Rev. Lett.* **1992**, *69*, 3314–3317.

[33] Houdré, R.; Stanley, R. P.; Oesterle, U.; Ilegems, M.; Weisbuch, C. *Phys. Rev. B* **1994**, *49*, 16761–16764.

[34] Houdré, R.; Weisbuch, C.; Stanley, R. P.; Oesterle, U.; Pellandini, P.; Ilegems, M. *Phys. Rev. Lett.* **1994**, *73*, 2043–2046.

[35] Agranovich, V.; Benisty, H.; Weisbuch, C. *Solid State Communications* **1997**, *102*, 631–636.

[36] Lidzey, D. G.; Bradley, D. D. C.; Skolnick, M. S.; Virgili, T.; Walker, S.; Whittaker, D. M. *Nature* **1998**, *395*, 53–55.

[37] Plumhof, J. D.; Stöferle, T.; Mai, L.; Scherf, U.; Mahrt, R. F. *Nature Materials* **2014**, *13*, 247–252.

[38] Cookson, T.; Georgiou, K.; Zasedatelev, A.; Grant, R. T.; Virgili, T.; Cavazzini, M.; Galeotti, F.; Clark, C.; Berloff, N. G.; Lidzey, D. G.; Lagoudakis, P. G. *Advanced Optical Materials* **2017**, *5*, 1700203.

[39] Kéna-Cohen, S.; Forrest, S. R. *Nature Photonics* **2010**, *4*, 371–375.

[40] Anoop, T.; Anjali, J.; Lucas, L.-K.; Robrecht, M. A. V.; Kalaivanan, N.; Eloise, D.; Cyriaque, G.; Joseph, M.; Thomas, W. E. *Nanophotonics* **2020**, *9*, 249–255.

[41] Campos-Gonzalez-Angulo, J. A.; Ribeiro, R. F.; Yuen-Zhou, J. *Nature Communications* **2019**, *10*, 4685.

[42] Du, M.; Ribeiro, R. F.; Yuen-Zhou, J. *Chem* **2019**, *5*, 1167–1181.

[43] Feist, J.; Galego, J.; Garcia-Vidal, F. J. *ACS Photonics* **2018**, *5*, 205–216.

[44] Felicetti, S.; Fregoni, J.; Schnappinger, T.; Reiter, S.; de Vivie-Riedle, R.; Feist, J. *The Journal of Physical Chemistry Letters* **2020**, *11*, 8810–8818.

[45] Fregoni, J.; Granucci, G.; Coccia, E.; Persico, M.; Corni, S. *Nature Communications* **2018**, *9*, 4688.

[46] Galego, J.; Garcia-Vidal, F. J.; Feist, J. *Physical Review X* **2015**, *5*, 041022.

[47] Galego, J.; Garcia-Vidal, F. J.; Feist, J. *Nature Communications* **2016**, *7*, 13841.

[48] Galego, J.; Garcia-Vidal, F. J.; Feist, J. *Physical Review Letters* **2017**, *119*, 136001.

[49] Herrera, F.; Spano, F. C. *Physical Review Letters* **2016**, *116*, 238301.

[50] Hirai, K.; Takeda, R.; Hutchison, J. A.; Uji-i, H. *Angewandte Chemie International Edition* **2020**, *59*, 5332–5335.

[51] Hutchison, J. A.; Schwartz, T.; Genet, C.; Devaux, E.; Ebbesen, T. W. *Angewandte Chemie International Edition* **2012**, *51*, 1592–1596.

[52] Lather, J.; Bhatt, P.; Thomas, A.; Ebbesen, T. W.; George, J. *Angewandte Chemie International Edition* **2019**, *58*, 10635–10638.

[53] Martínez-Martínez, L. A.; Ribeiro, R. F.; Campos-González-Angulo, J.; Yuen-Zhou, J. *ACS Photonics* **2018**, *5*, 167–176.

[54] Ribeiro, R. F.; Martínez-Martínez, L. A.; Du, M.; Campos-Gonzalez-Angulo, J.; Yuen-Zhou, J. *Chemical Science* **2018**, *9*, 6325–6339.

[55] Schwartz, T.; Hutchison, J. A.; Genet, C.; Ebbesen, T. W. *Physical Review Letters* **2011**, *106*, 196405.

[56] Thomas, A.; George, J.; Shalabney, A.; Dryzhakov, M.; Varma, S. J.; Moran, J.; Chervy, T.; Zhong, X.; Devaux, E.; Genet, C.; Hutchison, J. A.; Ebbesen, T. W. *Angewandte Chemie International Edition* **2016**, *55*, 11462–11466.

[57] Thomas, A.; Lethuillier-Karl, L.; Nagarajan, K.; Vergauwe, R. M. A.; George, J.; Chervy, T.; Shalabney, A.; Devaux, E.; Genet, C.; Moran, J.; Ebbesen, T. W. *Science* **2019**, *363*, 615.

[58] Vergauwe, R. M. A.; Thomas, A.; Nagarajan, K.; Shalabney, A.; George, J.; Chervy, T.; Seidel, M.; Devaux, E.; Torbeev, V.; Ebbesen, T. W. *Angewandte Chemie International Edition* **2019**, *58*, 15324–15328.

[59] Hertzog, M.; Rudquist, P.; Hutchison, J. A.; George, J.; Ebbesen, T. W.; Börjesson, K. *Chemistry – A European Journal* **2017**, *23*, 18166–18170.

[60] Hertzog, M.; Munkhbat, B.; Baranov, D.; Shegai, T.; Börjesson, K. *Nano Letters* **2021**, *21*, 1320–1326.

[61] Long, J. P.; Simpkins, B. S. *ACS Photonics* **2015**, *2*, 130–136.

[62] Hertzog, M.; Börjesson, K. *ChemPhotoChem* **2020**, *4*, 612–617.

[63] George, J.; Shalabney, A.; Hutchison, J. A.; Genet, C.; Ebbesen, T. W. *The Journal of Physical Chemistry Letters* **2015**, *6*, 1027–1031.

[64] Simpkins, B. S.; Fears, K. P.; Dressick, W. J.; Spann, B. T.; Dunkelberger, A. D.; Owrutsky, J. C. *ACS Photonics* **2015**, *2*, 1460–1467.

[65] Kapon, O.; Yitzhari, R.; Palatnik, A.; Tischler, Y. R. *The Journal of Physical Chemistry C* **2017**, *121*, 18845–18853.

[66] Saurabh, P.; Mukamel, S. *The Journal of Chemical Physics* **2016**, *144*, 124115.

[67] Menghrajani, K. S.; Fernandez, H. A.; Nash, G. R.; Barnes, W. L. *Advanced Optical Materials* **2019**, *7*, 1900403.

[68] Takele, W. M.; Wackenhut, F.; Piatkowski, L.; Meixner, A. J.; Waluk, J. *The Journal of Physical Chemistry B* **2020**, *124*, 5709–5716.

[69] Agranovich, V. M.; La Rocca, G. C. *Solid State Communications* **2005**, *135*, 544–553.

[70] Agranovich, V. M.; Litinskaia, M.; Lidzey, D. G. *Physical Review B* **2003**, *67*, 085311.

[71] Baieva, S.; Hakamaa, O.; Groenhof, G.; Heikkilä, T. T.; Toppari, J. J. *ACS Photonics* **2017**, *4*, 28–37.

[72] Grant, R. T.; Michetti, P.; Musser, A. J.; Gregoire, P.; Virgili, T.; Vella, E.; Cavazzini, M.; Georgiou, K.; Galeotti, F.; Clark, C.; Clark, J.; Silva, C.; Lidzey, D. G. *Advanced Optical Materials* **2016**, *4*, 1615–1623.

[73] Groenhof, G.; Climent, C.; Feist, J.; Morozov, D.; Toppari, J. J. *The Journal of Physical Chemistry Letters* **2019**, *10*, 5476–5483.

[74] Hulkko, E.; Pikker, S.; Tiainen, V.; Tichauer, R. H.; Groenhof, G.; Toppari, J. J. *The Journal of Chemical Physics* **2021**, *154*, 154303.

[75] Litinskaya, M. *Physics Letters A* **2008**, *372*, 3898–3903.

[76] Litinskaya, M.; Reineker, P.; Agranovich, V. M. *Journal of Luminescence* **2004**, *110*, 364–372.

[77] Somaschi, N.; Mouchliadis, L.; Coles, D.; Perakis, I. E.; Lidzey, D. G.; Lagoudakis, P. G.; Savvidis, P. G. *Applied Physics Letters* **2011**, *99*, 143303.

[78] Maxwell, J. C. *Philosophical Transactions of the Royal Society of London* **1865**, *155*, 459–512.

[79] Hertz, H. *Annalen der Physik* **1887**, *267*, 983–1000.

[80] Lewis, G. N. *Nature* **1926**, *118*, 874–875.

[81] Kavokin, A. V.; Baumberg, J. J.; Malpuech, G.; Laussy, F. P., *Microcavities*; Oxford University Press Inc.: 2007.

[82] Schrödinger, E. *Phys. Rev.* **1926**, *28*, 1049–1070.

[83] Atkins, P. W.; de Paula, J., *Physicalische Chemie*; Wiley-VCH: 2013.

[84] Mulliken, R. S. *Phys. Rev.* **1932**, *41*, 49–71.

[85] Morse, P. M. *Phys. Rev.* **1929**, *34*, 57–64.

[86] Jablonski, A. *Nature* **1933**, *131*, 839–840.

[87] Hollas, J. M., *Modern Spectroscopy*; Wiley & Sons Ltd: 2004.

[88] Atkins, P.; Friedmann, R., *Molecular Quantum Mechanics*; Oxford University Press: 2011.

[89] Dirac, P. A. M.; Fowler, R. H. *Proceedings of the Royal Society of London. Series A, Containing Papers of a Mathematical and Physical Character* **1928**, *117*, 610–624.

[90] Foldy, L. L.; Wouthuysen, S. A. *Phys. Rev.* **1950**, *78*, 29–36.

[91] Laporte, O.; Meggers, W. F. *J. Opt. Soc. Am.* **1925**, *11*, 459–463.

[92] Born, M.; Oppenheimer, R. *Annalen der Physik* **1927**, *389*, 457–484.

[93] Franck, J.; Dymond, E. G. *Trans. Faraday Soc.* **1926**, *21*, 536–542.

[94] Condon, E. *Phys. Rev.* **1926**, *28*, 1182–1201.

[95] Heisenberg, W. *Zeitschrift für Physik* **1927**, *43*, 172–198.

[96] Sen, D. *Current Science* **2014**, *107*, 203–218.

[97] Stoneham, A. M. *Rev. Mod. Phys.* **1969**, *41*, 82–108.

[98] Bellowsa), J. C.; Prasadb), P. N. *The Journal of Chemical Physics* **1979**, *70*, 1864–1871.

[99] Verhoeven, J. W. *Pure and Applied Chemistry* **1996**, *68*, 2223–2286.

[100] Kasha, M. *Discuss. Faraday Soc.* **1950**, *9*, 14–19.

[101] Dirac, P. A. M.; Bohr, N. H. D. *Proceedings of the Royal Society of London. Series A, Containing Papers of a Mathematical and Physical Character* **1927**, *114*, 243–265.

[102] Englman, R.; Jortner, J. *Molecular Physics* **1970**, *18*, 145–164.

[103] Siebrand, W. *The Journal of Chemical Physics* **1967**, *47*, 2411–2422.

[104] Parker, C. A.; Hatchard, C. G. *Trans. Faraday Soc.* **1961**, *57*, 1894–1904.

[105] Maciejewski, A.; Szymanski, M.; Steer, R. P. *The Journal of Physical Chemistry* **1986**, *90*, 6314–6318.

[106] Lakowicz, J. R., *Principles of Fluorescence Spectroscopy*; Springer: 2006.

[107] Braslavsky, S. E. *Pure and Applied Chemistry* **2007**, *79*, 293–465.

[108] Birks, J. B. *Reports on Progress in Physics* **1975**, *38*, 903–974.

[109] Musser, A. J.; Rajendran, S. K.; Georgiou, K.; Gai, L.; Grant, R. T.; Shen, Z.; Cavazzini, M.; Ruseckas, A.; Turnbull, G. A.; Samuel, I. D. W.; Clark, J.; Lidzey, D. G. *Journal of Materials Chemistry C* **2017**, *5*, 8380–8389.

[110] Ye, C.; Gray, V.; Kushwaha, K.; Kumar Singh, S.; Erhart, P.; Börjesson, K. *Physical Chemistry Chemical Physics* **2020**, *22*, 1715–1720.

[111] Ghosh, A.; Nakanishi, T. *Chemical Communications* **2017**, *53*, 10344–10357.

[112] Lu, F.; Nakanishi, T. *Science and Technology of Advanced Materials* **2015**, *16*, 014805.

[113] Lu, H.; Wang, Q.; Gai, L.; Li, Z.; Deng, Y.; Xiao, X.; Lai, G.; Shen, Z. *Chemistry – A European Journal* **2012**, *18*, 7852–7861.

[114] Kushwaha, K.; Yu, L.; Stranius, K.; Singh, S. K.; Hultmark, S.; Iqbal, M. N.; Eriksson, L.; Johnston, E.; Erhart, P.; Müller, C.; Börjesson, K. *Advanced Science* **2019**, *6*, 1801650.

[115] Müller, C. *Chemistry of Materials* **2015**, *27*, 2740–2754.

[116] Schäfer, C.; Mony, J.; Olsson, T.; Börjesson, K. *Chemistry – A European Journal* **2020**, *26*, 14295–14299.

[117] Chandrasekhar, S., *Radiative Transfer*; Dover Publications Inc.: 1960.

[118] Förster, T. *Annalen der Physik* **1948**, *437*, 55–75.

[119] Murphy, C. B.; Zhang, Y.; Troxler, T.; Ferry, V.; Martin, J. J.; Jones, W. E. *The Journal of Physical Chemistry B* **2004**, *108*, 1537–1543.

[120] Klán, P.; Wirz, J., *Photochemistry of Organic Compounds*; Wiley & Sons Ltd: 2009.

[121] Dexter, D. L. *The Journal of Chemical Physics* **1953**, *21*, 836–850.

[122] Förster, T. *Pure and Applied Chemistry* **1970**, *24*, 443–450.

[123] Stranius, K.; Börjesson, K. *Scientific Reports* **2017**, *7*, 41145.

[124] Irie, M.; Fukaminato, T.; Matsuda, K.; Kobatake, S. *Chemical Reviews* **2014**, *114*, 12174–12277.

[125] Bandara, H. M. D.; Burdette, S. C. *Chem. Soc. Rev.* **2012**, *41*, 1809–1825.

[126] Klajn, R. *Chem. Soc. Rev.* **2014**, *43*, 148–184.

[127] Dubonosov, A.; A. Bren, V.; Chernoivanov, V. *Russ. Chem. Rev.* **2002**, *71*, 917–927.

[128] Novotny, L. *American Journal of Physics* **2010**, *78*, 1199–1202.

[129] Landau, L.; Lifshity, E., *Quantum mechanics: non-relativistic theory*; Pergamon Press: 1977.

[130] Meystre, P.; Sargent, M., *Elements of Quantum Optics*; Springer: 1991.

[131] Grynberg, G.; Aspect, A.; Fabre, G., *Introduction to Quantum Optics*; Cambridge University Press: 2010.

[132] Törmä, P.; Barnes, W. L. *Reports on Progress in Physics* **2014**, *78*, 013901.

[133] Garraway, B. M. *Philosophical Transactions of the Royal Society A: Mathematical, Physical and Engineering Sciences* **2011**, *369*, 1137–1155.

[134] Dicke, R. H. *Phys. Rev.* **1954**, *93*, 99–110.

[135] Holstein, T.; Primakoff, H. *Phys. Rev.* **1940**, *58*, 1098–1113.

[136] Hopfield, J. J. *Phys. Rev.* **1958**, *112*, 1555–1567.

[137] Khitrova, G.; Gibbs, H. M.; Kira, M.; Koch, S. W.; Scherer, A. *Nature Physics* **2006**, *2*, 81–90.

[138] Agranovich, V. M.; Gartstein, Y. N.; Litinskaya, M. *Chemical Reviews* **2011**, *111*, 5179–5214.

[139] Skolnick, M. S.; Fisher, T. A.; Whittaker, D. M. *Semiconductor Science and Technology* **1998**, *13*, 645–669.

[140] Deng, H.; Haug, H.; Yamamoto, Y. *Rev. Mod. Phys.* **2010**, *82*, 1489–1537.

[141] Ebbesen, T. W. *Accounts of Chemical Research* **2016**, *49*, 2403–2412.

[142] Del Pino, J.; Feist, J.; Garcia-Vidal, F. J. *New Journal of Physics* **2015**, *17*, 053040.

[143] Coles, D. M.; Michetti, P.; Clark, C.; Adawi, A. M.; Lidzey, D. G. *Phys. Rev. B* **2011**, *84*, 205214.

[144] Grant, R. T.; Michetti, P.; Musser, A. J.; Gregoire, P.; Virgili, T.; Vella, E.; Cavazzini, M.; Georgiou, K.; Galeotti, F.; Clark, C.; Clark, J.; Silva, C.; Lidzey, D. G. *Advanced Optical Materials* **2016**, *4*, 1615–1623.

[145] Coles, D. M.; Michetti, P.; Clark, C.; Tsoi, W. C.; Adawi, A. M.; Kim, J.-S.; Lidzey, D. G. *Advanced Functional Materials* **2011**, *21*, 3691–3696.

[146] Schouwink, P.; Lupton, J. M.; von Berlepsch, H.; Dähne, L.; Mahrt, R. F. *Phys. Rev. B* **2002**, *66*, 081203.

[147] Munkhbat, B.; Wersäll, M.; Baranov, D. G.; Antosiewicz, T. J.; Shegai, T. *Science Advances* **2018**, *4*, eaas9552.

[148] Stranius, K.; Hertzog, M.; Börjesson, K. *Nature Communications* **2018**, *9*, 2273.

[149] Yu, Y.; Mallick, S.; Wang, M.; Börjesson, K. *Nature Communications* **2021**, *12*, 3255.

[150] Coles, D. M.; Somaschi, N.; Michetti, P.; Clark, C.; Lagoudakis, P. G.; Savvidis, P. G.; Lidzey, D. G. *Nature Materials* **2014**, *13*, 712–719.

[151] Zhong, X.; Chervy, T.; Wang, S.; George, J.; Thomas, A.; Hutchison, J. A.; Devaux, E.; Genet, C.; Ebbesen, T. W. *Angewandte Chemie International Edition* **2016**, *55*, 6202–6206.

[152] Georgiou, K.; Michetti, P.; Gai, L.; Cavazzini, M.; Shen, Z.; Lidzey, D. G. *ACS Photonics* **2018**, *5*, 258–266.

[153] Sáez-Blázquez, R.; Feist, J.; Fernández-Domınguez, A. I.; Garcıa-Vidal, F. J. *Phys. Rev. B* **2018**, *97*, 241407.

[154] Swann, S. *Physics in Technology* **1988**, *19*, 67–75.

Appendix